Elsevier Editorial System(tm) for Earth and Planetary Science Letters

Manuscript Draft

Manuscript Number:

Title: Origin and role of fluids involved in the seismic cycle of extensional faults in carbonate rocks

Article Type: Letters

Keywords: fluid circulation; seismic cycle; fluid pressure; stable isotopes; fault zone evolution; central Apennines

Corresponding Author: Dr. Luca Smeraglia, M.D.

Corresponding Author's Institution: Sapienza Università di Roma

First Author: Luca Smeraglia, M.D.

Order of Authors: Luca Smeraglia, M.D.; Fabrizio Berra, Prof; Andrea Billi, DR; Chiara Boschi, DR; Eugenio Carminati, Prof; Carlo Doglioni, Prof

Abstract: Structural and geochemical methods applied to the seismically-active extensional Tre Monti Fault (central Apennines, Italy) were used to develop a conceptual evolutionary model of seismic faulting with fluid involvement for shallow (≤ 3 km depth) extensional faults in carbonate rocks. Multiscale fault rock structures such as injection veins, fluidized ultracataclasite layers as well as crackle and chaotic breccias were recognized and interpreted in terms of seismic cycle. The relative chronology of these structures was reconstructed through cross-cutting relationships and cathodoluminescence analyses. C- and O-isotope data from different generations of fault-related mineralizations show a shift from marine- to meteoric-derived fluid circulation during exhumation from 3 to ≤1 km depths and concurrent fluid cooling from ~68 to <35 °C. Between ~3 km and ~1 km depths, impermeable barriers within the sedimentary sequence created a semi-closed hydrological system, where marine-derived fluids circulated within the fault zone at temperatures between 60° and 75°C without any mixing with meteoric-derived fluids. During fault zone exhumation at depths ≤ 1 km and temperatures <35 °C, the hydrological circulation became open and meteoric-derived fluids progressively infiltrated and circulated within the fault zone. The role of these geofluids during syn-exhumation seismic cycles of the TMF has been substantially passive along the whole fault zone, with the fluids being passively redistributed at hydrostatic pressure following co-seismic dilatancy. Only the principal fault has been characterized, locally and transiently, by fluid overpressures. The presence of low-permeability clayey layers in the sedimentary sequence contributed to control the type of fluids infiltrating into the fault zone and possibly their transient overpressures. These results can foster the comprehension of seismic faulting at shallow depths in carbonate rocks of other fold-thrust belts involved in post-collisional seismogenic extensional tectonics.

Suggested Reviewers: Perach Nuriel Dr
Geological Surveys of Israel

pnuriel@hotmail.com
Expert of fluids and earthquakes

Tonguc Uysal Prof
University of Queensland, Australia, + Ankara University
t.uysal@uq.edu.au
Expert in fluids and earthquake

Thomas Mitchell Dr
University College London
tom.mitchell@ucl.ac.uk
Expert in fault mechanics and earthquake

Lori Kennedy Prof
The University of British Columbia
lkennedy@eos.ubc.ca
Expert of fluids and earthquakes

Anne-Marie Boullier Prof
University Joseph Fourier, Grenoble 1, France
anne-marie.boullier@ujf-grenoble.fr
Expert in fluids and earthquakes

Opposed Reviewers:

Rome, 15/10/2015

Dear Editor,

Please, find enclosed the material concerning the manuscript entitled “Origin and role of fluids involved in the seismic cycle of extensional faults in carbonate rocks” by Luca Smeraglia et alii. We would be very grateful if you could consider this manuscript for its possible publication on Earth and Planetary Science Letters.

We propose a study of a major extensional fault zone (Tre Monti fault) from the Central Apennines (Italy), combining different methods such as geological mapping, structural analyses, optical microscopy, cathodoluminescence, carbon and oxygen stable isotopes, and whole rock geochemistry. We address, in particular, the origin and temperatures of fluid circulating within the fault zone and their role at different depths in terms of fluid pressure fluctuations during the seismic cycle. From this case history, we develop a general conceptual model (Fig. 10) for seismically-active shallow ($\leq$ 3 km depth) extensional faults cutting through heterogeneous sedimentary sequence (i.e., carbonate rocks and siliciclastic sandstones with clayey intercalations).

Our study brings to the community a conceptual model that can promote a better comprehension of fluid-fault interactions at shallow depths in carbonate rocks. Moreover, the proposed model can be valid elsewhere as the stratigraphic and tectonic setting of the Central Apennines is similar to other seismically active fold-thrust belts characterized by post-collisional extension and exhumation.

The submitted material is wholly original and has not been published or is not under consideration for publication elsewhere.

The manuscript includes ten figures and three additional tables as supplementary material.

With Best Regards

Luca Smeraglia and co-authors

Highlights

Stratigraphy and fault structures influence fault-related fluid circulation

Between ~3 and ~1 km depths marine-derived fluids circulated within the fault zone

At depths ≤ 1 km meteoric-derived fluids infiltrated into the fault zone

Fluids were redistributed at hydrostatic pressure following co-seismic dilatancy

Only the principal fault has been characterized by fluid overpressures

*Manuscript
Click here to view linked References

Origin and role of fluids involved in the seismic cycle of extensional faults in carbonate rocks

Luca Smeraglia[1*], Fabrizio Berra[2], Andrea Billi[3], Chiara Boschi[4], Eugenio Carminati[1, 3], and Carlo Doglioni[1,3]

1. Dipartimento di Scienze della Terra, Sapienza Università di Roma, P.le Aldo Moro 5, 00185 Roma, Italy

2. Università degli Studi di Milano, Dipartimento di Scienze della Terra, Via Mangiagalli 34, 20133 Milano, Italy

3. Consiglio delle Nazionale Ricerche, IGAG, c.o. Dipartimento di Scienze della Terra, Sapienza Università di Roma, P.le Aldo Moro 5, 00185 Roma, Italy

4. Istituto di Geoscienze e Georisorse, Consiglio Nazionale delle Ricerche, Via Moruzzi 1, 56124 Pisa, Italy

Luca Smeraglia: luca.smeraglia@uniroma1.it

Fabrizio Berra: fabrizio.berra@unimi.it

Andrea Billi: andrea.billi@cnr.it

Chiara Boschi: c.boschi@igg.cnr.it

Eugenio Carminati: eugenio.carminati@uniroma1.it

Carlo Doglioni: carlo.doglioni@uniroma1.it

* Corresponding author: Dipartimento di Scienze della Terra, Sapienza Università di Roma, Piazzale Aldo Moro 5, 00185 Roma, Italy. Tel.: +39 06 49914156

E-mail address: luca.smeraglia@uniroma1.it (Luca Smeraglia)

Abstract: Structural and geochemical methods applied to the seismically-active extensional Tre Monti Fault (central Apennines, Italy) were used to develop a conceptual evolutionary model of seismic faulting with fluid involvement for shallow (≤ 3 km depth) extensional faults in carbonate rocks. Multiscale fault rock structures such as injection veins, fluidized ultracataclasite layers as well as crackle and chaotic breccias were recognized and interpreted in terms of seismic cycle. The relative chronology of these structures was reconstructed through cross-cutting relationships and cathodoluminescence analyses. C- and O-isotope data from different generations of fault-related mineralizations show a shift from marine- to meteoric-derived fluid circulation during exhumation from 3 to ≤1 km depths and concurrent fluid cooling from ~68 to <35 °C. Between ~3 km and ~1 km depths, impermeable barriers within the sedimentary sequence created a semi-closed hydrological system, where marine-derived fluids circulated within the fault zone at temperatures between 60° and 75°C without any mixing with meteoric-derived fluids. During fault zone exhumation at depths ≤ 1 km and temperatures <35 °C, the hydrological circulation became open and meteoric-derived fluids progressively infiltrated and circulated within the fault zone. The role of these geofluids during syn-exhumation seismic cycles of the TMF has been substantially passive along the whole fault zone, with the fluids being passively redistributed at hydrostatic pressure following co-seismic dilatancy. Only the principal fault has been characterized, locally and transiently, by fluid overpressures. The presence of low-permeability clayey layers in the sedimentary sequence contributed to control the type of fluids infiltrating into the fault zone and possibly their transient overpressures. These results can foster the comprehension of seismic faulting at shallow depths in carbonate rocks of other fold-thrust belts involved in post-collisional seismogenic extensional tectonics.

Keywords: fluid circulation, seismic cycle, fluid pressure, stable isotopes, fault zone evolution, central Apennines

1. Introduction

Fluid flow along faults has been widely explored for implications on various topics including hydrocarbon and ore exploration, CO_2 sequestration, groundwater and contaminant transport, and faulting (e.g., Cox, 1995; Williams et al., 2015). Faults and fault zones are not only preferential conduits or barriers for the passage of geofluids, but their slip is often modulated by the fluids themselves (e.g., Keranen et al., 2013).

Fluids have been suggested to play either passive or active roles during the seismic cycle (e.g., Sibson, 2014; Fig. 1). For instance, the "fault-valve" model (Fig. 1a) involves an active role of overpressured fluids that can trigger earthquakes (e.g., Miller et al., 2004; Haney et al., 2005). After seismic failure, fluid discharge and sealing mineralizations are favored by hydrofracturing and decompression (stress drop), respectively (e.g., Cox, 1995). Complete fracture sealing allows fluid overpressure to build again and initiate a new seismic cycle. This mechanism can commonly act within fluid-overpressured crustal blocks (e.g., Di Luccio et al., 2010) especially along subduction interfaces, where fluid overpressure is more likely to develop and be sustained (Sibson, 2014). On the other hand, different scenarios involve a passive role of fluids that are redistributed following an earthquake (e.g., Sibson, 2000). Fluid redistribution can be favored by rapid co-seismic dilation and creation of high-permeability fracture networks characterized by subhydrostatic pressure (Fig. 1b, "suction-pump" model) or by crack closure favored by post-seismic stress recovery (Fig. 1c, "mean stress cycling" model). If low-permeability barriers are not created, fluids conserve hydrostatic pressure. These mechanisms can easily act within extensional/transtensional regimes (e.g., Doglioni et al., 2013; Sibson, 2014) in the shallow crust (<5 km), where hydrostatic fluid pressure and high permeability zones have been documented (Townend and Zoback, 2000). Such scenarios can be validated studying footprints left by fluids, such as seismic-related mineralizations and rock fluid structures and textures (e.g., Uysal et al., 2009; Rowe and Griffith, 2015). Therefore, the study of the geological record of fluid-fault interactions is a fundamental pre-requisite for general models

78 concerning the origin and role of fluids involved in the seismic cycle. Single case histories are
79 fundamental to build comprehensive conceptual models of seismic-related fluid circulation.
80 We here propose a case study of a major extensional fault (Tre Monti Fault, TMF, central
81 Apennines, Italy) from a carbonate domain in the central Apennines, Italy (Fig. 2a). The study of
82 this fault is relevant as, at shallow crustal levels (< 10 km depth), fault zones in carbonate rocks
83 represent favorable structures for migration and entrapment of geofluids (e.g., Ghisetti et al., 2001).
84 Moreover, in many seismically active regions worldwide (including our study area), shallow crustal
85 earthquakes and seismic sequences (e.g., hypocenters at < 10 km depth) nucleate in and propagate
86 upward through carbonate rocks with fluids involvement in the seismic cycle (e.g., Macedonia,
87 Greece, 1995, M_w 6.6 earthquake, Stiros, 1995; Wenchuan, China, 2008, M_w 8.0 earthquake, Chen
88 et al., 2013; L'Aquila, Italy, 2009, M_w 6.3 earthquake, Chiaraluce, 2012).
89 The TMF, which exhumed from depth ≤ 3 km since about Pliocene time (Galadini et al., 2003),
90 is presently characterized by excellent exposures allowing geoscientists to study the relationships
91 between fault zone architecture, fluid circulation, and seismic cycle within a tectonically active
92 extensional setting (Smith et al., 2011). As many earthquakes frequently cause surface ruptures and
93 associated damage and fatalities (Stiros, 1995; Galli et al., 2009), the study of such a shallow fault
94 is relevant for the understanding of the fault zone architecture and fluid circulation at shallow
95 depths (≤ 3 km).
96 Our main aim is to synthesize the spatio-temporal tectonic evolution and fluid circulation of the
97 TMF into a conceptual model of seismic-related fluid circulation within shallow (≤ 3 km)
98 extensional fault zones. To do so, we combine structural, microstructural, and geochemical
99 (cathodoluminescence, stable isotopes, and whole rock geochemistry) methods. The main novelty
100 of this model concerns the origin of geofluids involved in the seismic cycle of exhuming
101 extensional fault zones and their specific role, which is substantially passive along most part of the
102 fault zone except along the principal fault, where fluid overpressures can locally arise during co-
103 seismic phases.

2. Geological Setting

2.1. Apennines evolution and seismotectonic setting

The Central Apennines are a late Oligocene-to-Present fold-and-thrust belt related to the west directed subduction and eastward rollback of the Adriatic under the European plate (e.g., Doglioni, 1991). Shortening was characterized by the northeastward migration of thrust fronts in a classical forelandward piggy-back sequence of thrust sheets (Cosentino et al., 2010). These tectonic processes brought carbonates onto syn-orogenic deposits along NW-SE-oriented thrust faults (Fig. 2a; Cosentino et al., 2010). The thrust sheets consist of ~4-5 km thick Late Triassic-Middle Miocene shallow-water carbonate rocks, whereas the syn-orogenic deposits consist of up to ~3 km thick Late Miocene hemipelagic marls and deep-marine siliciclastic sandstones with intercalated clayey layers (Cosentino et al., 2010).

Since Late Miocene time, while the compressional deformation was still active along the eastern fronts (Adriatic domain), the Apennines belt underwent extension in its western and axial parts. Normal faulting led to crustal thinning related to the development of the Tyrrhenian backarc basin (Doglioni, 1991). This process is still active and has generated a system of NW-SE-oriented basin-bounding active extensional faults and perpendicular strike- to oblique-slip transfer faults (Fig. 2a). Both sets of faults produced large historical and instrumental earthquakes up to M_w 7 (Fig. 2a; e.g., Avezzano, 1915, M_w 7.0 earthquake; L'Aquila, 2009, M_w 6.3 earthquake; Galli et al., 2008; Chiaraluce, 2012). The TMF belongs to this active tectonic setting representing a transfer fault between two NW-SE-oriented extensional faults (Morewood and Roberts, 2000).

In the Apennines, the imbricated carbonates and syn-orogenic sequences can be traced from the surface to depths of ca. 8–10 km (Patacca et al., 2008). Although some mainshocks could nucleate within the underlying crystalline basement (~10 km depth), it is well documented that many foreshocks and aftershocks as well as some mainshocks nucleated and propagated within the overlying sedimentary sequence (Miller et al., 2004; Ventura and Di Giovambattista, 2013). For

example, during the 2009 L'Aquila earthquake sequence, large foreshocks and aftershocks (up to M_w 5.5) nucleated at < 5 km depth. Fluid-earthquake interactions at different crustal levels have been instrumentally documented for the most recent earthquakes of the region. For instance, near lithostatic fluid pressure at hypocentral depth triggered both the mainshocks and the aftershocks during the M_w 6.0, 1997 Colfiorito (Miller et al. 2004) and M_w 6.3, 2009 L'Aquila (Di Luccio et al. 2010) earthquakes. Malagnini et al., (2012) suggested that, during the L'Aquila earthquake, pore fluid pressure diffusion was responsible for the spatial migration of seismicity with the activation of different fault segments.

In the Apennines, earthquakes frequently ruptured the Earth's surface (e.g., Galli et al., 2009; Benedetti et al., 2013). In this way, the fluids that circulate at shallow crustal levels into groundwater aquifers (< 1 km depth) can enter into and interact within the fault zone. For instance, the L'Aquila earthquake also influenced hydrochemical and hydrological groundwater circulation (Amoruso et al., 2011; Doglioni et al., 2013).

2.2. The Tre Monti Fault

The TMF marks the north-western boundary of the Fucino basin, which is an intra-mountain half-graben filled by Late Pliocene–Quaternary continental deposits (Fig. 2b; Cavinato et al., 2002). Paleoseismological investigations suggest that the TMF has been active between Early Pliocene and present times (i.e., in post-orogenic times; e.g., Benedetti et al., 2013). The TMF is exposed for a length of ~8 km along the southern slope of the Tre Monti Hills as an almost continuous series of ENE-WSW-oriented and SSE-dipping fault surfaces and scarps in Mesozoic limestones (Fig. 2b).

Based on stratigraphic offset and kinematic indicators, the TMF can be defined as an extensional fault with some evidence of transtensional right-lateral slip (e.g., Morewood and Roberts, 2000). Seismic cross-sections through the TMF indicate that the cumulative throw increases from ~0.7 km in the western part to ~2 km in the eastern part (Fig. 2c, Cavinato et al., 2002; Patacca et al., 2008).

156 The TMF displaces the Tre Monti anticline, an open fold of Mesozoic-Cenozoic carbonate
157 deposits and Late Tertiary syn-orogenic deposits with a north-western periclinal termination (Fig.
158 3a). The pre-orogenic carbonates crop out for a thickness of ~600 m and are unconformably
159 overlain by syn-orogenic deposits with a minimum thickness of ~150 m (Fig. 3a). Vitrinite
160 reflectance data indicate that, in this area, the syn-orogenic deposits were buried to maximum
161 depths of up to 2 km (Corrado et al., 2010). As the tectonic activity of the TMF started both after
162 the compressional deformation and after the deposition of syn-orogenic deposits, we infer that the
163 exposed portion of the TMF was exhumed from depth ≤ 3 km.
164
165 **3. Structural and Cathodoluminescence Data**
166 *3.1. Methods*
167 The following methods were applied to unravel the TMF architecture:
168 (1) Original field mapping (at 1:5,000 scale or larger), aerial photographs and high resolution
169 digital elevation models allowed us to reconstruct the surface kilometric-scale geometry of the
170 TMF,
171 (2) We constructed two geological cross-sections through the TMF to calculate fault
172 displacements and investigate the buried structure. The sections are constrained by field and seismic
173 reflection data.
174 (3) We conducted detailed structural analyses and systematic sampling within La Forchetta
175 quarry to reconstruct the fault zone internal architecture,
176 (4) We analyzed fault-rock micro-structures in fifty-two oriented thin sections using optical
177 microscopy to investigate the deformation mechanisms,
178 (5) We used cathodoluminescence microscopy (CL) employing a cold cathode luminoscope
179 (Nuclide ELM2; e.g., Berra et al., 2012) to distinguish the different phases of fluid-related
180 mineralizations.
181

3.2. Fault zone setting and general architecture

The TMF is segmented into up to eleven SSE-dipping (45°-65°) fault segments (Fig. 3a). A buried fault segment occurs at the foot of the Tre Monti hills as inferred by seismic reflection data (Cavinato et al., 2002; Fig. 3a). The principal fault surface coincides with the most downhill fault scarp, and juxtaposes carbonate rocks in the footwall with both syn-orogenic marine and post-orogenic continental deposits in the hangingwall (Figs. 3b and 3c). The latter deposits consist of subaerial slope debris composed by carbonate clasts cemented by calcite precipitates.

The principal fault is exposed along a series of en-echelon parallel fault scarps, whereas other segments are buried and inferred by morphological evidence (scarps interpreted as tectonically-controlled) within the continental deposits (Fig. 3a). The principal fault accommodates most of displacement (Figs. 3b and 3c). The fault surfaces are commonly striated by sets of slickenlines indicating two main movements: transtensional right-lateral (Fig. 3d) and extensional dip-slip (Fig. 3e). We observed no overprinting relationships between slip indicators. A set of secondary synthetic faults is hosted in the carbonate bedrock behind the principal fault (Figs. 3b and 3c). These faults are characterized by displacements up to a few hundreds of meters (Figs. 3b and 3c).

The La Forchetta quarry is located within a stepover between two en-echelon principal fault segments cutting Early Cretaceous shallow-water carbonates, which include two alternating facies: 1) peritidal white limestone and 2) oolithic grey limestone. In the quarry and nearby areas, as shown in the conceptual cross-section through the fault zone, we identify three main structural domains (Fig. 4a): principal fault (domain 1, D1); damage zone (domain 2, D2); secondary fault zone (domain 3, D3). We describe the three domains in detail as follows.

3.3. Principal fault (D1)

The principal fault (Figs. 4a and 4b) accommodates ~1500 m of throw and concentrates most shear deformation through a fault core that is up to ~1 m thick (Fig. 5a). The fault core consists of ultracataclasite and foliated cataclasite (Fig. 5b).

(1) The ultracataclasite lies below the principal fault surface forming discontinuous patches and plagues with pinch-out geometry above the underlying foliated cataclasite (Fig. 5b). The boundary between the two fault rocks is sharp and continuous (Fig. 5c) or, alternatively, is marked by small, bulbous protrusions of ultracataclasite into the underlying foliated cataclasite, resembling fluid-like structures (Fig. 5c). The ultracataclasite is brownish (Fig. 5c) and up to ~20 cm thick. Clasts from the foliated cataclasite (between 0.1 and 10 mm in diameter, Figs. 5c and 6a) are dispersed within a ground mass composed by ultrafine-grained material (<0.1 mm in diameter, Fig. 6a). Calcite cement pervades the ultracataclasite. The cement is characterized by a low dull red CL color (Fig. 6b), whereas the clasts and the ultrafine-grained material show black luminescence (Fig. 6b).

(2) The foliated cataclasite is grey (Fig. 5c) and up to ~80 cm thick. The foliation is marked by a series of cataclastic shear zones (~0.25 mm thick, Fig. 6c), which encase sigmoids and clasts of host rock affected by extensional microfractures (Fig. 6d). Also in this case, calcite cement pervades the foliated cataclasite. The cement, which represents the groundmass of the foliations (dark in transmitted light), and the extensional microfractures are characterized by dull red color under CL light (Figs. 6g and 6i).

Within the above-described ultracataclasite and foliated cataclasite, we recognized the following structures:

(1) Extensional fractures filled by fine-grained granular material cutting across the foliated cataclasite, often branching out from the ultracataclasite (Fig. 4a). Based on their geometry, we call these filled fractures as granular injections. They form a complex network with sharp boundaries (Fig. 6e). Randomly oriented, angular to subangular reworked fragments from the ultracataclasite and/or foliated cataclasite are dispersed throughout the ultrafine matrix of the injections defining a massive and unsorted texture (Figs. 6g and 6i). Under CL light, two sets of granular injections can be recognized: set 1 has cement with dull red CL color (Fig. 6g), whereas set 2 has cement with bright red CL color (Fig. 6i). Set 2 systematically cuts across set 1 (Fig. 6g).

(2) Type 1 veins (T1 veins) are randomly oriented calcite-filled veins < 100 μm thick with discontinuous and/or branching geometry that can be recognized only under CL light. T1 veins often branch out from set 2 injections (Fig. 6i) and cut across both the ultracataclasite and the foliated cataclasite (Figs. 6b and 6i). Vein filling is composed by anhedreal and equant calcite crystals < 30 μm in diameter with blocky texture. Crystals do not show growth competition textures and smooth boundaries form triple junctions textures (Fig. 6j). No CL zoning is observed within these crystals that have the same bright red CL color of set 2 granular injections (Fig. 6k). The same fluid probably precipitated the clacite of both T1 veins and set 1 granular injections.

(3) Type 2 veins (T2 veins) are up to 1 mm thick extensional calcite-filled veins that are often located in steps and rhomb-shaped pull-apart structures along small Riedel shear fractures (R and P fractures; Fig. 5c). These veins are characterized by sharp boundaries (Fig. 6l), whereas the filling is composed by subhedral calcite crystals up to 200 μm in size with elongate-blocky textures. Growth competition textures (e.g., Hilgers et al., 2004) are common with growth directions perpendicular to vein walls (Fig. 6l). T2 veins are characterized by no luminescence under CL light (Fig.6i) and cut across (i.e., postdate) all the previously described structures (Fig.6i). We recognized T2 veins also within D2 and D3 (Fig. 4a).

3.4. Damage zone (D2)

Within the damage zone (Figs. 4a and 4b), which is ~60 m thick, deformation is heterogeneously distributed through calcite-filled veins, patches of joints, and low-displacement (< 3 m) faults (Figs. 4a and 4b). These structures are described as follows.

(1) Type 3 veins (T3 veins) are calcite-filled extensional veins up to 1 mm thick and a few centimeters long (Fig. 7a). The veins are widespread within the entire damage zone with various orientations. Different sets crosscut each other, creating an intersecting network of calcite filled veins (Fig. 7a). The resulting texture is a crackle-like breccia (Figs. 7b and 7f) similar to those described by Woodcock et al. (2014) in carbonate rocks. The crystals filling these veins (Fig. 7b)

are characterized by black luminescence under CL light and by textures similar to T2 veins (D1). In D2, we also recognized T2 veins, which systematically cut across T3 veins (Fig. 4a). T3 veins are absent in D1 and present in D3 (Fig. 4a).

(2) Joints are frequent in D2 with a wide range of orientations. The most continuous and penetrative set is subvertical and WNW-ESE-oriented (plot 1 in Fig. 4c). Joints are not filled and are spaced between 0.5 and 10 cm. They delimit prismatic rock fragments (Fig. 7c) and cut across both T2 and T3 veins (Fig. 4a). Joints are substantially absent in D1.

(3) Low-displacement faults are characterized by two main strikes (N90° and N170°) with slickenlines indicating oblique-slip and extensional dip-slip motions (plots 2, 5, and 6 in Fig. 4c). Faults surfaces are well striated and often coated with reddish calcite slickenfibers (Fig. 7d). Small breccia bodies, with the same characteristics of that described in the next section, are interposed along fault planes. Faults and joints are characterized by mutual crosscutting relationships and both cut across T2 and T3 veins (Fig. 4a). Low-displacement faults are also present in D3 and absent in D1.

3.5. Secondary fault zone (D3)

The secondary fault zone (Figs. 4a and 4b) consists of a ~30 m long, ~15 m high, and up to ~5 m thick zone of deformation, accommodating a ~50 m of total throw. The zone contains parallel fault segments encasing the following structures.

(1) The best-exposed fault segment (Fig. 7e) is oriented WNW-ESE with slickenlines indicating strike- and oblique-slip movements (plots 3 and 4 in Fig. 4c). This fault, as well as other fault surfaces both in D2 and D3, is well striated and often coated with reddish calcite slickenfibers (Fig. 7d).

(2) In D3, we recognized T2 and T3 veins, and joints. T2 veins systematically cut through T3 veins, and both these veins (T2 and T3) are cut by both the fault surfaces and the joints.

(3) Foliated breccias (Fig. 8a) cemented by calcite are present within D3 (Fig. 7e). They rest above striated fault surfaces (Fig. 8b) and often fill subvertical, NW-SE-oriented extensional fracture zones, which are up to 5 cm wide (Fig. 8c). The boundaries between breccias and both fault surfaces and fracture walls are sharp. Foliations within these breccias consist of undulated, sharp, and striated fault surfaces, which are about parallel to low-displacement faults (Figs. 8a and 8b). Breccias exhibit a chaotic texture (Fig. 8d; classification of Woodcock et al., 2014) with numerous voids. Clasts are randomly oriented, angular to subangular, and ranging from <0.1 up to 10 cm in diameter. Several clasts are characterized by inner crackle breccia textures (Fig. 8d). Within the clasts, we recognized T2 and T3 veins (Fig. 8d). Breccias are cemented by reddish calcite precipitates, which occur in two different generations. Generation 1 cement (G1) consists of blocky to elongate-blocky calcite crystals up to 200 μm in diameter. This cement fill fractures between clasts (Figs. 8e and 8f). Generation 2 cement (G2) consists of acicular calcite crystals up to 1 mm in length, forming fibrous cement. The G2 cement wraps around both the carbonate clasts and the G1 cement (Figs. 8e and 8f). The breccia is clast-supported, with clasts usually surrounded by the G1 and/or G2 cements. "Sealing hiatuses" (sensu Nuriel et al., 2012) between G1 and G2 cements are common (Figs. 8e and 8f). Both the G1 and G2 cements show black luminescence under CL light.

We synthetize all the previous described mesostructures, microstructures, cathodoluminescence data, and crosscutting relationships of domain 1, 2, and 3 in Table S1.

4. Stable Isotope data and whole rock geochemistry

4.1. Method and sampling strategy

To determine both the origin and the temperature of (parental) fluids from which the $CaCO_3$ precipitates derived, we analyzed the C- and O-isotope signatures ($\delta^{13}C$ and $\delta^{18}O$) of 78 samples collected from the TMF domains and nearby rocks (e.g., Vannucchi et al., 2010). We carried out these analyses using a mass spectrometer (Finnigan MAT Delta Plus) equipped with Finnigan Gas-Bench II at the Institute of Geosciences and Earth Resources (IGG, CNR, National Research

310 Council, Pisa, Italy). Results are reported according to the conventional δ notations Vienna Pee Dee
311 Belemnite (PDB) and Vienna Standard Mean Ocean Water (SMOW) (Fig. 9a and Table S2). We
312 verified a mean external reproducibility better than 0.1 both for $\delta^{13}C$ and for $\delta^{18}O$.
313 The analyzed samples are from the ultracataclasite and foliated cataclasite (9 samples,
314 "cataclastic rocks" in Fig. 9a), T2 and T3 veins (18 samples, "T2 veins" and 9 samples, "T3 veins"
315 in Fig. 9a), G1 and G2 cement of breccia (25 samples, "breccia cements" in Fig. 9a), and calcite
316 slickenfibers on fault surfaces (4 samples, "calcite slickenfibers" in Fig. 9a). We also analyzed the
317 Cretaceous host rocks sampled outside the fault zone (9 samples, "host rock" in Fig. 9a) and the
318 cement within the post-orogenic Quaternary continental deposits (4 samples, "Quaternary deposits
319 cement" in Fig. 9a). We used the isotopic values from Cretaceous host rocks and Quaternary
320 deposits as a reference for comparison with values obtained from the rocks sampled within the TMF
321 zone.
322 Concerning T2 and T3 veins (< 1 mm thick), we extracted the material for isotope analyses
323 using a microdrill equipped with spikes down to 0.3 mm in diameter. On the contrary, we were not
324 able to sample T1 veins (D1), as they are too thin (< 100 μm thick) to be sampled without
325 significant contamination from the surrounding rock.
326 To determine the chemical composition of cataclastic rocks from D1 (ultracataclasite and
327 foliated cataclasite) and host rock, we commissioned an external laboratory (www.actlabs.com) the
328 whole rock geochemistry on 6 samples (Fig. 9b, 2 from the ultracataclasite, 2 from the foliated
329 cataclasite, and 2 from the host rock). The detection limits of all elements and the complete
330 analyses are available in Table S3.
331
332 *4.2. Results*
333 Results from the stable isotope analyses and whole rock geochemistry are shown in Figs. 9a
334 and 9b, respectively, and listed in Table S2 and Table S3, respectively. The following features can
335 be recognized:

(1) Host rock: $\delta^{13}C$ and $\delta^{18}O$ values range between -0.8‰ and 2.4‰, and 26‰ and 31‰, respectively. Geochemical analyses indicate isotope values and Sr concentrations similar to those of most Cretaceous marine carbonates in central Italy (e.g., Agosta and Kirchner, 2003).

(2) Quaternary deposits cement: $\delta^{13}C$ and $\delta^{18}O$ range between -8.7‰ and -9.3‰, and 24.4‰ and 24.9‰, respectively.

(3) Cataclastic rocks (ultracataclasite and foliated cataclasite, D1): $\delta^{13}C$ and $\delta^{18}O$ range between -0.1‰ and 0.8‰, and 23.2‰ and 24.4‰, respectively. The $\delta^{18}O$ average value is depleted by about 4.5‰ with respect to the host rock. Geochemical analyses indicate Sr concentrations higher than that of the host rock. As the cataclastic rocks developed mechanically recycling the host rock and involving authigenic precipitation of calcite cement, the $\delta^{18}O$ values and Sr concentrations are a mixture of both host-rock and authigenic calcite (i.e., they cannot be physically separated). It follows that true $\delta^{18}O$ values and Sr concentrations of these rocks should be lower and higher, respectively, than that measured.

(4) T2 veins (D1, D2, and D3): $\delta^{13}C$ and $\delta^{18}O$ range between -2.9‰ and -8.2‰, and 22.8‰ and 25.8‰, respectively.

(5) T3 veins (D2 and D3): $\delta^{13}C$ and $\delta^{18}O$ range between -0.4‰ and 1.6‰, and 21.6‰ and 27‰, respectively. The $\delta^{18}O$ average value is depleted by about 4.2‰ with respect to the host rock.

(6) Calcite slickenfibers (D2 and D3): $\delta^{13}C$ and $\delta^{18}O$ range between -5‰ and -7.8‰, and 24.1‰ and 24.4‰, respectively.

(7) Breccia cements (D3): $\delta^{13}C$ and $\delta^{18}O$ range between -8.9‰ and -10.2‰, and 24.2‰ and 25.4‰, respectively.

5. Discussion

5.1 Fluid Sources

Potential sources of the fluids producing the O- and C-isotope compositions measured in the studied samples include: (1) meteoric water; (2) groundwater circulating in carbonate aquifers; (3)

362 marine and connate waters trapped into carbonates and syn-orogenic deposits; (4) fluids derived
363 from dehydration and metamorphic decarbonation reactions within the subducting sediments and
364 crystalline basement of the Adriatic crust; (5) deep-seated fluids (> 10 km depth) enriched in CO_2
365 from mantle degassing (e.g., Ghisetti et al., 2001).

366 Discriminating among these sources is critical for the development of a correct model of fluid
367 flow in this and similar tectonic contexts. We acknowledge that, being both the exact temperature
368 and the O isotope composition of the parental fluids unknown, such discrimination can be non
369 unique. To partly solve this problem, we discuss different hypotheses under the reasonable
370 assumptions that calcite precipitated in the 0-3 km depth and 5°-100°C temperature ranges as
371 constrained both by geological and organic matter maturity data (Corrado et al., 2010). Based on
372 these assumptions, two sources of fluids are identified for different fault rocks/veins of the TMF.

373 (a) Marine-derived brines and/or connate waters: Considering the range of isotope values of
374 both cataclastic rocks (D1) and T3 veins (D2-D3), as a first hypothesis, we assume that the fluid
375 responsible for calcite precipitation consisted of brines and/or connate waters derived from marine
376 water trapped within the syn-orogenic deposits and carbonate rocks. Some pieces of evidence
377 corroborate this hypothesis:

378 (1) the $\delta^{13}C$ values (PDB) ranging from 0‰ to 2 ‰ (Fig. 9a) exclude external fluids such as
379 meteoric and/or groundwater ($\delta^{13}C$ < -5‰), deep-seated (0‰ < $\delta^{13}C$ > -5‰), or decarbonation
380 ($\delta^{13}C$ > 5‰) derived fluids;

381 (2) Sr concentration within ultracataclasite (D1) is higher than that of marine carbonates of the
382 host rock (Fig. 9b) and of fault-related precipitates from meteoric-derived water in the same region
383 (Agosta and Kirschner, 2003) and in other areas (e.g., Williams et al., 2015). The Sr concentration
384 is higher in ultracataclasite than in foliated cataclasite owing to higher cement content in the
385 ultracataclasite. Although the cataclastic rocks derived from the mechanical recycling of host rock,
386 the high Sr content of authigenic calcite cement within ultracataclasite is evident. Such a high Sr

content is consistent with calcite cement precipitated from very high-salinity fluids such as brines and/or connate waters;

(3) bright and dull luminescence of calcite precipitates within cataclastic rocks indicate their precipitation in reducing (rich in Mn^{2+}) and confined environments (Nuriel et al., 2011), such as marine water trapped within low-permeability ultracataclasite.

To verify the fluid source and know the precipitation environment (i.e., depth), we calculated the mineralizing fluid temperatures using the equation of Kele et al., (2015) for inorganic calcite precipitation in the 6°-95°C temperature range, assuming calcite precipitation in equilibrium with marine-like fluid. As benchmark $\delta^{18}O$, we used the $\delta^{18}O$ value of marine water (0‰ SMOW). We assume that the marine water preserved its isotopic composition as a relatively large amount of pore water was retained in the rocks and relatively little exchange occurred between the pore water and surrounding rocks prior to vein precipitation. The calculated temperature of precipitation is in the 60° to 75°C range (average value of ~68°C), equivalent to a maximum burial depth of ~2.5 km for the TMF (i.e., assuming a geothermal gradient of 30°C/km consistent with an immature extensional tectonic setting).

An alternative hypothesis consists of a fluid partially or entirely rock-buffered in its isotopic composition. Such a condition does not allow the determination of fluid source(s) through isotope analyses, but only indicates that the fluid equilibrated with the host rock. In this latter case, the $\delta^{18}O$ and $\delta^{13}C$ of the newly precipitated calcite should be nearly equal to the values of the host rocks, as suggested by Ghisetti et al., (2001) studying calcite precipitates along thrusts of the Apennines. Such a scenario is not consistent with our data, as the average $\delta^{18}O$ values (SMOW) of the cataclastic rocks and T3 veins are depleted by ~4.5‰ with respect to the host rock. In addition, the relatively narrow range of $\delta^{13}C$ values (0‰ and +2‰ PDB) is inconsistent with values characteristic of marine carbonates (between -2‰ and +4 ‰ PDB). Finally, the precipitation temperatures calculated using $\delta^{18}O$ values of a fluid in equilibrium with the host rock are unlikely

high (305° to 470°C). We therefore reject this alternative hypothesis and indicate the scenario involving brines and/or connate waters trapped within pores as the most suitable.

(b) Meteoric-derived fluid: The range of isotope values of T2 veins (D1-D2-D3), calcite slickenfibers (D2-D3), and breccia cements (D3) (Fig. 9a) are consistent with calcite precipitated from a meteoric-derived fluid that circulated trough organic rich soils and then into carbonates groundwater aquifers before infiltrating within the fault zone at shallow depth (≤1 km). The $\delta^{13}C$ values (PDB) are lower than -4‰, typical of C-organic imprinting (mostly C_3-type vegetation) and are similar to that of groundwater measured in carbonate aquifers (e.g., Falcone et al., 2008). The isotopic values of T2 veins (D1-D2-D3), calcite slickenfibers (D2-D3), and breccia cements (D3) are consistent with those of Quaternary breccia cements, unequivocally deposited near the surface in continental environment. Also in this case, we calculated the mineralizing fluid temperatures considering calcite precipitation in equilibrium with meteoric-derived fluids ($\delta^{18}O$ from -10‰ to -5‰ SMOW; Craig, 1961). Results indicate low precipitation temperatures between 6.5° and 35°C. This large temperature range is due to the high variability of $\delta^{18}O$ values for meteoric waters. However, the calculated temperatures are consistent with in situ temperatures of groundwater aquifers at <1 km depth (e.g., Pasquale et al., 2013).

Based on the previous considerations, we interpret the studied mineralizations as derived from parental fluids consisting of either marine-derived fluids (brine and/or connate water trapped within stratigraphic units) or meteoric- and/or groundwater-derived fluids.

5.2. Spatio-temporal evolution of fault zone architecture and fluid flow

We combine crosscutting relationships, cathodoluminescence evidence, and geochemical data from the TMF to propose a general model for the spatio-temporal evolution and fluid circulation within the shallow portions (≤ 3 km depth) of a carbonate-hosted seismogenic fault. We identify two phases of fault zone evolution:

(a) After the compressional phase characterized by folding and thrusting, the Apennines belt experienced post-collisional extension, exhumation, and seismicity at its rear and within its axial zone (Doglioni, 1991; Fig. 10a). Based on the crosscutting relationships, the first structures produced at depth ≤ 3 km were cataclastic rocks (ultracataclasite and foliated cataclasite) within the principal fault (D1) and T3 veins in the damage zone (D2-D3) (Fig. 10b). Deformation was strongly concentrated in the narrow principal fault, whereas fracturing and veining generated broad and less intense deformation within the damage zone. The cumulative displacement (> 1 km) accommodated by the principal fault allowed the juxtaposition of marine syn-orogenic deposits and carbonates. Therefore, brines and/or connate waters trapped within syn-orogenic deposits flowed laterally into D1 (Fig. 10b). In addition, similar fluids trapped within carbonates flowed vertically and laterally into D2 and D3 (Fig. 10b). Low-permeability barriers (i.e., clayey layers) within the syn-orogenic deposits did not allow mixing of connate and external (i.e., meteoric- and/or groundwater-derived fluids) fluids (Fig. 10b). The difference in luminescence between calcite precipitates within cataclastic rocks (D1; bright and dull) and T3 veins (D2 and D3; black) possibly indicate a difference in the redox conditions within precipitation environments and/or slightly different composition of the trapped fluid within the syn-orogenic deposits respect to that within the carbonate rocks. In this latter case, D1 provided a permeability barrier to fluid flow toward D2 and D3. This kind of fluid circulation indicates semi-closed hydrological conditions as documented in other extensional (e.g., Williams et al., 2015) and compressional tectonic settings (e.g., Ghisetti et al., 2001; Kirschner and Kennedy, 2001; Vannucchi et al., 2010)

(b) In the late stage of fault zone development, the exposed portion of the TMF was exhumed to depth ≤ 1 km by uplift and erosion of the Apennines belt (Galadini et al., 2003). Owing to low confining pressure, deformation was distributed over a broader volume of the damage zone, where patches of joints (D2-D3), breccias (D3), and veins (T2 veins) developed (Fig. 10c). Tectonically controlled scarps within continental deposits (Fig. 3a) confirm a widening of the fault zone at

462 shallow depths. Displacement was no more accommodated only by D1, but also by low-
463 displacement faults cutting through the damage zone (D2-D3; Fig. 10c).

464 During exhumation, the TMF intersected shallow (< 1 km depth) groundwater aquifers,
465 connected with the Earth's surface (Fig. 10c). Therefore, meteoric- and/or groundwater-derived
466 fluids infiltrated downward into the fault zone, as showed by isotope values of T2 veins (D1-D2-
467 D3), calcite slickenfibers (D2-D3), and breccia cements (D3). Moreover, black luminescence of all
468 these structures indicates near surface and well oxygenated precipitation environments (Fig. 10c).
469 This evidence involves open hydrological conditions in connection with groundwater aquifers as
470 documented in the same region (e.g., Agosta and Kirschner, 2003) and in other tectonic settings
471 (e.g., Menzies et al., 2014) also in connection with seismic sequences (Amoruso et al., 2011;
472 Doglioni et al., 2013).

473

474 *5.3. Fluid involvement in the seismic cycle*

475 In this section, we discuss a model for fluid circulation, fluid pressure fluctuations, and fluid
476 redistribution during concurrent exhumation and seismic activity within the shallow portion (≤ 3 km
477 depth) of active fault zones in carbonate rocks, such as the TMF.

478 (a) Inter-seismic phase: The high permeability networks of fractures and breccias of the TMF
479 allowed the maintenance of hydrostatic fluid pressure up to a depth of ~3 km within critically-
480 stressed faults (e.g., Townend and Zoback, 2000). Fluid pressure was essentially at hydrostatic
481 value between ~3 km and ~1 km depth and at depth ≤ 1 km within the whole fault zone (Figs. 10d
482 and 10e).

483 (b) Co-seismic phase: the crackle-like breccia texture and the chaotic texture of foliated
484 breccias indicate numerous events of co-seismic dilatancy, brecciation, and collapse of crackle
485 breccia clasts into fault voids along dilational sites (e.g., Woodcock et al., 2014). Cataclasis and
486 shearing, which generated foliation planes within breccias, may have been either synchronous with
487 co-seismic slip, or associated with aseismic creep (e.g., Stünitz et al., 2010). We propose that

488 extensional fractures and dilation within the damage zone between ~3 km and ~1 km depth (D2 and
489 D3; Fig. 10d) and within the whole fault zone at depth ≤ 1 km (D1, D2, and D3; Fig., 10e) occurred
490 by co-seismic dilatancy at hydrostatic fluid pressure both by rapid tensile pulses propagation (e.g.,
491 Ben-Zion and Shi, 2005) and by dilatancy along fault dilational jogs (e.g., Sibson, 2000) rather than
492 by hydrofracturing at near-lithostatic fluid pressure. As tensile strength is small for most
493 sedimentary rocks (1-10 MPa), extensional fracturing and dilatancy can occur down to ~3-4 km
494 depth at hydrostatic fluid pressure (e.g., Sibson, 2000). Even if overpressured fluids were generated
495 at depths of ~5-10 km (e.g., Miller et al., 2004; Haney et al., 2005; Di Luccio et al., 2010), these
496 overpressures could not be sustained during their upward propagation within high permeability
497 fracture networks and breccias of shallow fault zones (Townend and Zoback, 2000). Thus,
498 hydrofracturing was improbable at shallow crustal depths (≤ 3 km). Immediately after co-seismic
499 dilatancy, the fluid pressure dropped toward subhydrostatic values into newly created extensional
500 fractures allowing the suction of fluids into fractures, CO_2 partial pressure drop and exsolution, and
501 calcite precipitation from a suprasaturated solution (e.g., Uysal et al., 2009; Figs. 10d and 10e).
502 However, we found evidence indicating that transient overpressures were only localized into the
503 principal fault (D1) when the fault was active between ~3 km and ~1 km depth (Fig. 10d). Granular
504 injections show texture of injections veins similar to those described by Lin, (2011), indicating that
505 fluid and ultrafine granular material became fluidized to form a solid-liquid system, which was
506 squeezed into the complex network of extensional hydrofractures created by overpressured fluids.
507 Moreover, we interpret fluid-like structures (Fig. 5c) similar to those found at smaller scales in the
508 TMF by Smith et al., (2011) as the result of fluidization of granular material that probably occurred
509 by overpressured fluids release. In addition, calcite crystal textures in T1 veins indicate very high
510 calcite precipitation rate (e.g., Boullier et al., 2004). This is due to large CO_2 pressure drop and
511 exsolution as, at low temperatures (< 100 °C), the larger the CO_2 pressure drop and exsolution, the
512 higher the calcite precipitation rate. Large pressure drops likely occurred during fall from

513 suprahydrostatic fluid pressure (i.e., near-lithostatic) to hydrostatic fluid pressure within newly
514 created hydrofractures (Fig. 10d).
515 (c) Post-seismic phase: After co-seismic dilatancy, fluids were passively redistributed at
516 hydrostatic pressure level trough the newly created network of high permeable extensional fractures
517 and breccias (Figs. 10d and 10e). Microstructures of calcite filled veins indicate that extensional
518 fractures remained open at hydrostatic pressure conditions until sealing. Vein filling shows
519 subhedral crystals with growth competition textures, indicating that crystals slowly precipitated into
520 fluid-filled and open spaces with continuous advection of suprasaturated solution (e.g., Hilgers et
521 al., 2004). Estimated growth rates of natural calcite crystals in tectonic veins precipitated at non-
522 equilibrium conditions range between 10^{-1} and 10^{-2} mm/a (Uysal et al., 2009; Frery et al., 2015).
523 Veins from TMF are up to 1 mm wide, thus they may have been sealed in a few years or months
524 and even less for thinner veins. Localized and transient fluid pressure (e.g., Hadizadeh et al., 2012)
525 cannot maintain extensional fracture open for such times.
526
527 **6. Conclusions**
528 We integrated geological mapping and structural analyses together with cathodoluminescence
529 and geochemical investigations to propose, from a single case history, a conceptual model of
530 seismic fault zone evolution. In the studied case, the stratigraphic-structural setting and burial-
531 exhumation history involved the presence of different types of geofluids (i.e., marine- and meteoric-
532 derived), which have actively or passively assisted the seismic cycle. Between ~3 km and ~1 km
533 depths and temperatures between 60° and 75°C, marine-derived fluids trapped within syn-orogenic
534 deposits and carbonate rocks, respectively, in the hangingwall and footwall, circulated within the
535 fault zone. Semi-closed hydrological circulation, created by low-permeability barriers within the
536 syn-orogenic deposits (i.e., clayey layers), did not allow mixing with meteoric-derived fluid. During
537 co-seismic dilatancy, fluid pressure shifted toward sub-hydrostatic values in the damage zone and
538 toward an overpressure state along the principal fault, where overpressured fluids actively assisted

539 the co-seismic slip promoting hydrofracturing and granular fluidization. During the post-seismic
540 phase, fluids were passively re-distributed at hydrostatic pressure. With the progressive exhumation
541 toward depths ≤ 1 km, the hydrological circulation became open due to the interaction with
542 groundwater aquifers. Meteoric-derived fluids infiltrated and circulated within the fault zone at
543 temperatures ≤ 35°C. At these depths, fluid pressure shifted from subhydrostatic to hydrostatic
544 values during co-seismic and post-seismic phase, respectively, without fluid overpressure
545 occurrences.

546 We assess that the proposed model of seismic fluid-fault interaction can be valid elsewhere as
547 the stratigraphic and tectonic setting of the Central Apennines is similar to other seismically active
548 fold-thrust belts characterized by post-collisional extension and exhumation. We point out, in
549 particular, the role played by low-permeability compartments that can modulate the type of fluids
550 infiltrating into the fault zone at various levels of exhumation.

551

552 **Acknowledgements**

553 Financial support from PRIN2010/11 (Project 20107ESMX9 "Crisi e ripresa di sistemi carbonatici
554 e potenziale per la formazione di reservoir: i ruoli di clima, tettonica e magmatismo") and Progetti
555 di Ateneo (Sapienza) 2012 and 2014 led by Carlo Doglioni and Eugenio Carminati is
556 acknowledged. Francesca Castorina, Andrea Cavallo, Cristiano Collettini, Giulio Di Toro, Michele
557 Fondriest, and Steve Smith are thanked for fruitful discussions. Domenico Mannetta is thanked for
558 thin section preparation. Ilaria Baneschi and Simone Vezzoni are thanked for help during sample
559 preparation and isotope analyses.

560

561 **References**

562 Agosta, F., Kirschner, D.L., (2003). Fluid conduits in carbonate-hosted seismogenic normal faults
563 of central Italy. Journal of Geophysical Research 108, 2221, doi: 10.1029/2002JB002013.

564 Amoruso, A., Crescentini, L., Petitta, M., Rusi, S., Tallini, M., (2011). Impact of the 6 April 2009
565 L'Aquila earthquake on groundwater flow in the Gran Sasso carbonate aquifer, Central Italy.
566 Hydrological Processes 25, 1754-1764, doi: 10.1002/hyp.7933.
567 Ben-Zion, Y., Shi, Z., (2005). Dynamic rupture on a material interface with spontaneous generation
568 of plastic strain in the bulk. Earth and Planetary Science Letters 236, 486-496, doi:
569 10.1016/j.epsl.2005.03.025.
570 Benedetti, L., Manighetti, I., Gaudemer, Y., Finkel, R., Malavieille, J., Pou, K., Maurice, A.,
571 Aumaitre, G., Bourlès, D., Keddadouche, K., (2013). Earthquake synchrony and clustering on
572 Fucino faults (Central Italy) as revealed from in situ ^{36}Cl exposure dating. Journal of
573 Geophysical Research 118, 4948-4974, doi: 10.1002/jgrb.50299, 2013.
574 Berra, F., Balini, M., Levera, M., Nicora, A., Salamati, R., (2012). Anatomy of carbonate mounds
575 from the Middle Anisian of Nakhlak (Central Iran): architecture and age of a subtidal
576 microbial-bioclastic carbonate factory. Facies 58, 685-705, doi: 10.1007/s10347-012-0299-z.
577 Boullier, A. M., Fujimoto, K., Ohtani, T., Roman-Ross, G., Lewin, E., Ito, H., Pezard, P., Ildefonse,
578 B. (2004). Textural evidence for recent co-seismic circulation of fluids in the Nojima fault
579 zone, Awaji island, Japan. Tectonophysics 378, 165-181, doi: 10.1016/j.tecto.2003.09.006.
580 Cavinato G.P., Carusi C, Dall'Asta M, Miccadei E, Piacentini T., (2002). Sedimentary and tectonic
581 evolution of Plio–Pleistocene alluvial and lacustrine deposits of Fucino Basin (central Italy).
582 Sedimentary Geology 148, 29-59, PII: S0037-0738(01)00209-3.
583 Chen, J., Yang, X., Ma, S., Spiers, C.J. (2013). Mass removal and clay mineral
584 dehydration/rehydration in carbonate‐rich surface exposures of the 2008 Wenchuan
585 Earthquake fault: Geochemical evidence and implications for fault zone evolution and
586 coseismic slip. Journal of Geophysical Research 118, 474-496, doi: 10.1002/jgrb.50089.
587 Chiaraluce, L., (2012). Unravelling the complexity of Apenninic extensional fault systems: A
588 review of the 2009 L'Aquila earthquake (Central Apennines, Italy). Journal of Structural
589 Geology 42, 2-18, doi: 10.1016/j.jsg.2012.06.007.

590 Corrado, S., Aldega, L., Zattin M., (2010). Sedimentary vs. tectonic burial and exhumation along
591 the Apennines (Italy). In: Beltrando, M., Peccerillo, A., Mattei, M., Conticelli, S., Doglioni,
592 C., (Eds.), The Geology of Italy, Journal of the Virtual Explorer 36, Electronic Edition, paper
593 15, 1-37, doi: 10.3809/jvirtex.2010.00232.
594 Cosentino, D., Cipollari P., Marsili P., Scrocca, D., (2010). Geology of the central Apennines: a
595 regional review. In: Beltrando, M., Peccerillo, A., Mattei, M., Conticelli, S., Doglioni, C.,
596 (Eds.), Journal of the Virtual Explorer 36, paper 12, 1-36, doi: 10.3809/jvirtex.2010.00223.
597 Cox, S.F., (1995). Faulting processes at high fluid pressures: an example of fault valve behavior
598 from the Wattle Gully Fault, Victoria, Australia. Journal of Geophysical Research 100, 12841-
599 12859.
600 Craig, H., (1961). Isotopic variations in meteoric waters. Science 133, 1702-1703.
601 Di Luccio, F., Ventura, G., Di Giovambattista, R., Piscini, A., Cinti, F.R., (2010). Normal faults and
602 thrusts reactivated by deep fluids: The 6 April 2009 Mw 6.3 L'Aquila earthquake, central
603 Italy. Journal of Geophysical Research 115, 1-15, doi: 10.1029/2009JB007190.
604 Doglioni, C., (1991). A proposal for the kinematic modelling of W-dipping subductions; possible
605 applications to the Tyrrhenian-Apennines system. Terra Nova 3, 423-434.
606 Doglioni, C., Barba S., Carminati E., Riguzzi F., (2013). Fault on-off versus coseismic fluids
607 reaction. Geoscience Frontiers 5, 767-780, doi: 10.1016/j.gsf.2013.08.004.
608 Falcone, R.A., Falgiani, A., Parisse, B., Petitta, M., Spizzico, M., Tallini M., (2008). Chemical and
609 isotopic ($\delta^{18}O‰$, $\delta^{2}H‰$, $\delta^{13}C‰$, ^{222}Rn) multi-tracing for groundwater conceptual model of
610 carbonate aquifer (Gran Sasso INFN underground laboratory–central Italy). Journal of
611 hydrology 357, 368-388, doi: 10.1016/j.jhydrol.2008.05.016.
612 Frery, E., Gratier, J.P., Ellouz-Zimmerman, N., Loiselet, C., Braun, J., Deschamps, P., Blamart, D.,
613 Hamelin, B., Swennen, R., (2015). Evolution of fault permeability during episodic fluid
614 circulation: Evidence for the effects of fluid–rock interactions from travertine studies (Utah–
615 USA). Tectonophysics 651, 121-137, doi: 10.1016/j.tecto.2015.03.018

616 Galadini, F., Messina P., Giaccio B., Sposato, A., (2003). Early uplift history of the Abruzzi
617 Apennines (central Italy): available geomorphological constraints, Quaternary International
618 101-102, 125–135, doi: 10.1016/S1040-6182(02)00095-2.
619 Galli, P., Galadini, F. and D., Pantosti, (2008). Twenty years of paleoseismology in Italy. Earth
620 Science Review 88, 89-117, doi: 10.1016/j.earscirev.2008.01.001.
621 Galli, P., Camassi, R., Azzaro, R., Bernardini, F., Castenetto, S., Molin, D., Peronace, E., Rossi, A.,
622 Vecchi, M., Tertulliani, A., (2009). Terremoto de L'Aquila del 6 aprile 2009: Rilievo
623 macrosismico, distribuzione delle intensità macrosismiche ed implicazioni sismotettoniche. Il
624 Quaternario 22.
625 Ghisetti, F., Kirschner, D.L., Vezzani, L., Agosta, F., (2001). Stable isotope evidence for
626 contrasting paleofluid circulation in thrust faults and normal faults of the central Apennines,
627 Italy. Journal of Geophysical Research 106, 8811-8825.
628 Hadizadeh, J., Mittempergher, S., Gratier, J.P., Renard, F., Di Toro, G., Richard, J., Babaie, H.A.,
629 (2012). A microstructural study of fault rocks from the SAFOD: Implications for the
630 deformation mechanisms and strength of the creeping segment of the San Andreas Fault.
631 Journal of Structural Geology 42, 246-260, doi: 10.1016/j.jsg.2012.01.011.
632 Haney, M.M., Snieder, R., Sheiman, J., Losh, S., (2005). Geophysics: A moving fluid pulse in a
633 fault zone. Nature 437, 46-46, doi: 10.1038/437046.
634 Hilgers, C., Dilg-Gruschinski, K., Urai, J.L., (2004). Microstructural evolution of syntaxial veins
635 formed by advective flow, Geology 32, 261-264, doi: 10.1130/G20024.1.
636 Kele, S., Breitenbach, S.F.M., Capezzuoli, E., Nele Meckler, A., Ziegler, M., Millan, I.M., Kluge,
637 T., Deák, J., Hanselmann, K., John, C.M., Yan, H., Liu, Z., Bernasconi, S.M., (2015).
638 Temperature dependence of oxygen- and clumped isotope fractionation in carbonates: a study
639 of travertines and tufas in the 6-95°C temperature range. Geochimica et Cosmochimica Acta
640 168, 172-192, doi: 10.1016/j.gca.2015.06.032.

641 Keranen, K.M., Savage, H.M., Abers, G.A., Cochran, E.S. (2013). Potentially induced earthquakes
642 in Oklahoma, USA: Links between wastewater injection and the 2011 Mw 5.7 earthquake
643 sequence. Geology 41, 699-702, doi: 10.1130/G34045.1.
644 Kirschner, D.L., Kennedy, L.A. (2001). Limited syntectonic fluid flow in carbonate- hosted thrust
645 faults of the Front Ranges, Canadian Rockies, inferred from stable isotope data and structures.
646 Journal of Geophysical Research 106, 8827-8840, doi: 10.1029/2000JB900414.
647 Lin, A., (2011). Seismic slip recorded by fluidized ultracataclastic veins formed in a coseismic
648 shear zone during the 2008 MW 7.9 Wenchuan earthquake. Geology 39, 547-550, doi:
649 10.1130/G32065.1.
650 Malagnini, L., Lucente, F.P., De Gori, P., Akinci, A., Munafo, I., (2012). Control of pore fluid
651 pressure diffusion on fault failure mode: Insights from the 2009 L'Aquila seismic sequence.
652 Journal of Geophysical Research 117, B05302., doi: 10.1029/2011JB008911.
653 Menzies, C.D., Teagle, D.A., Craw, D., Cox, S.C., Boyce, A.J., Barrie, C.D., Roberts, S., (2014).
654 Incursion of meteoric waters into the ductile regime in an active orogen. Earth and Planetary
655 Science Letters 399, 1-13, doi: 10.1016/j.epsl.2014.04.046.
656 Miller, S.A., Collettini, C., Chiaraluce, L., Cocco, M., Barchi, M., Kaus, B.J.P., (2004). Aftershocks
657 driven by a high-pressure CO_2 source at depth. Nature 427, 724-727, doi:
658 10.1038/nature02251.
659 Morewood, N., Roberts, G.P (2000). The geometry, kinematics and rates of deformation within an
660 en échelon normal fault segment boundary, central Italy. Journal of Structural Geology 22,
661 1027-1047, PII: S0191-8141(00)00030-4.
662 Nuriel, P., Rosenbaum, G., Uysal, I.T., Zhao, J.-X., Golding, S.D., Weinberger, R., Karabacak, V.,
663 Avni, Y., (2011). Formation of fault-related calcite precipitates and their implications for
664 dating fault activity in the East Anatolian and Dead Sea fault zones. In: Fagereng, Å., et al.,
665 (eds), Geology of the earthquake source: A volume in honour of Rick Sibson: The Geological
666 Society of London Special Publication 359, 229–248, doi: 10.1144/SP359.13.

667 Nuriel, P., Weinberger, R., Rosenbaum, G., Golding, S.D., Zhao, J.-X., Uysal, I.T., Bar-Matthews,
668 M., Gross, M.R., (2012). Timing and mechanism of late-Pleistocene calcite vein formation
669 across the Dead Sea Fault Zone, northern Israel. Journal of Structural Geology 36, 43–54, doi:
670 10.1016/j.jsg.2011.12.010.
671 Pasquale, V., Chiozzi, P., Verdoya, M., (2013). Evidence for thermal convection in the deep
672 carbonate aquifer of the eastern sector of the Po Plain, Italy. Tectonophysics 594, 1-12, doi:
673 10.1016/j.tecto.2013.03.011.
674 Patacca, E., Scandone P., Di Luzio E., Cavinato G.P., Parotto, M. (2008). Structural architecture of
675 the central Apennines: Interpretation of the CROP 11 seismic profile from the Adriatic coast
676 to the orographic divide. Tectonics 27, tc3006, doi:10.1029/2005tc001917.
677 Rowe, C.D., Griffith, W.A., (2015). Do Faults Preserve a Record of Seismic Slip: A second
678 opinion. Journal of Structural Geology 78, 1-26, doi: 10.1016/j.jsg.2015.06.006.
679 Sibson, R.H., (2000). Fluid involvement in normal faulting. Journal of Geodynamics 29, 469-499,
680 PII: S0264-3707(99)00042-3.
681 Sibson, R.H. (2014). Earthquake Rupturing in Fluid-Overpressured Crust: How Common? Pure and
682 Applied Geophysics 171, 2867-2885, doi: 10.1007/s00024-014-0838-3.
683 Smith, S.A.F., Billi, A., Di Toro, G., Spiess, R., (2011). Microstructures of Principal Slip Zones in
684 Limestones, and Implications for the Seismic Cycle (Tre Monti fault, central Appennines,
685 Italy). Pure and Applied Geophysics 168, 2365-2393, doi: 10.1007/s00024-011-0301-7.
686 Stiros, S., (1995). Unexpected shock rocks an ‘aseismic’ area. Eos, Transactions American
687 Geophysical Union 76, 513-519, doi: 10.1029/95EO00316.
688 Stünitz, H., Keulen, N., Hirose, T., Heilbronner, R. (2010). Grain size distribution and
689 microstructures of experimentally sheared granitoid gouge at coseismic slip rates–Criteria to
690 distinguish seismic and aseismic faults?. Journal of Structural Geology 32, 59-69, doi:
691 doi:10.1016/j.jsg.2009.08.002.

692 Townend, J., Zoback, M.D., (2000). How faulting keeps the crust strong. Geology 28, 399-402, doi:
693 10.1130/0091-7613.
694 Uysal, I.T., Feng, Y., Zhao, J.X., Isik, V., Nuriel, P., Golding, S.D., (2009). Hydrotermal CO_2
695 degassing in seismically active zones during the Late Quaternary. Chemical Geology 265,
696 442-454, doi: 10.1016/j.chemgeo.2009.05.011.
697 Vannucchi, P., Remitti, F., Bettelli, G., Boschi, C., Dallai, L., (2010). Fluid history related to the
698 early Eocene ‐ middle Miocene convergent system of the Northern Apennines (Italy):
699 Constraints from structural and isotopic studies. Journal of Geophysical Research 115, 1978-
700 2012, 115, doi: 10.1029/2009JB006590.
701 Ventura, G., Di Giovambattista, R., (2013). Fluid pressure, stress field and propagation style of
702 coalescing thrusts from the analysis of the 20 May 2012 ML 5.9 Emilia earthquake (Northern
703 Apennines, Italy). Terra Nova 25, 72-78, doi: 10.1111/ter.12007.
704 Williams, R.T., Goodwin, L.B., Mozley, P.S., Beard, B.L., Johnson, C.M., (2015). Tectonic
705 controls on fault zone flow pathways in the Rio Grande rift, New Mexico, USA. Geology 43,
706 723-726, doi: 10.1130/G36799.1.
707 Woodcock, N.H., Miller A.V.M., Woodhouse, C.D. (2014). Chaotic breccia zones on the Pembroke
708 Peninsula, south Wales: Evidence for collapse into voids along dilational faults. Journal of
709 Structural Geology 69, 91-107, doi: 10.1016/j.jsg.2014.09.019.
710

711 **Figure captions**

712

713 **Figure 1.** Different models of interactions between fluids and seismic cycle. **(a)** Fault-valve action.
714 **(b)** Suction-pump action. **(c)** Mean stress cycling. Modified after Sibson (2000).

715

716 **Figure 2. (a)** Simplified geological map of the central Apennines (Italy), showing main thrusts and
717 active normal faults. The inset shows a schematic tectonic setting of central-southern Italy with
718 main thrusts and active normal faults. **(b)** Geological setting of the Fucino basin and Tre Monti
719 Fault (TMF) (Cavinato et al., 2002). **(c)** Seismic reflection cross-sections (left cross-section:
720 data line drawing and interpretation; right cross-section: data and interpretation) through the
721 TMF (Cavinato et al., 2002; Patacca et al., 2008). Cross-section traces are shown in (b).

722

723 **Figure 3. (a)** Geological map of the TMF area along the northern boundary of the Fucino basin.
724 The inset shows the stratigraphic-structural relationships in the area. **(b)** and **(c)** Geological
725 cross-sections through the TMF and topographic renditions of the Tre Monti Hills. Cross-
726 section traces in (a). **(d)** Schmidt net (lower hemisphere) showing attitude of meso-scale fault
727 surfaces and related slip vectors (right-lateral transtensional movements). **(e)** Schmidt net
728 (lower hemisphere) showing attitude of meso-scale fault surfaces and related slip vectors (dip-
729 slip extensional movements).

730

731 **Figure 4. (a)** Simplified conceptual cross-section through the TMF within La Forchetta quarry,
732 showing the crosscutting relationships and three main structural domains: (principal fault, D1;
733 damage zone, D2; secondary fault zone, D3). This figure represents our index reference for
734 what concerns the three studied structural domains, their spatial distribution, and the
735 crosscutting relationships between structures within each domain (see also Table S1). **(b)**
736 Frontal view of La Forchetta quarry (photograph above and line drawing below), showing

exposures of the main structural domains. **(c)** Simplified structural map of La Forchetta quarry. Schmidt nets (lower hemisphere) show attitude of joints (plot 1) and low displacement faults with related slip vectors (plots from 2 to 6). Quarry location: Latitude 42°04'36" N, Longitude 13°29'59" E.

Figure 5. Fault structures in the principal fault (domain 1, D1). **(a)** Overview of the principal fault surface, which juxtapose Cretaceous carbonate deposits in the footwall with Plio-Pleistocene continental deposits in the hangingwall. **(b)** Cross-sectional view of the principal fault surface and ~100 cm thick cataclastic fault core. The ultracataclasite forms discontinuous patches over the foliated cataclasite. **(c)** High resolution scan of a hand sample cut perpendicularly to the principal fault surface and parallel to slip direction. The boundary between ultracataclasite and foliated cataclasite is sharp and continuous, but often marked by undulations, protrusions, and fluid-like structures.

Figure 6. Microphotographs of the principal fault (domain 1, D1) structures taken from thin sections under plane polarized light (PPL), crossed polarized light (CPL), and/or cathodoluminescence light (CL). **(a)** Texture of the ultracataclasite (PPL). Note the clasts from the foliated cataclasite dispersed within the ultrafine-grained matrix forming the ultracataclasite. **(b)** Same as previous microphotograph under CL. Calcite cement has dull red luminescence whereas T1 vein has bright red luminescence. **(c)** Cataclastic foliation and host rock clasts within the foliated cataclasite (CPL). **(d)** Host rock clasts within the foliated cataclasite with extensional microfractures forming a jigsaw puzzle texture (CPL). **(e), (f)** Granular injections filled by ultrafine material. Note that the injections cut through the foliated cataclasite (PPL). **(g)** Same as previous microphotograph (f) under CL. Set 2 granular injection has bright red luminescence and cuts across set 1 granular injection, which has dull red luminescence. T1 veins have bright red luminescence and branch out from set 2 granular

763 injection, whereas extensional microfractures have dull red luminescence and branch out from
764 set 1 granular injections. **(h)** Granular injections filled by ultrafine material. (PPL). **(i)** Same as
765 previous microphotograph under CL. Note the massive and unsorted texture of the granular
766 injection. Both set 2 granular injection and T1 veins have bright red luminescence and cut
767 across the foliated cataclasite. T2 vein has no luminescence and cuts across the foliated
768 cataclasite, T1 veins, and set 2 granular injection. **(j)** Anhedral, blocky calcite crystals
769 characterized by boundaries with triple-junctions. These crystals fill T1 veins (PPL, insets
770 under CPL). **(k)** Same as previous microphotograph under CL. Calcite crystals have bright red
771 luminescence and no CL zoning. **(l)** Elongate-blocky calcite crystals within T2 veins. Arrows
772 indicate growth direction and sense of vein crystals (CPL).
773
774 **Figure 7.** Photographs and microphotographs of the damage zone (domain 2, D2) and of the
775 secondary fault zone (domain 3, D3) structures. **(a)** High resolution hand sample scan (D2)
776 including T3 veins. **(b)** Microphotograph of T3 veins (D2) taken under crossed polarized light.
777 T3 veins are characterized by elongate-blocky calcite crystals and by mutual crosscutting
778 relationships. Arrows indicate growth direction and sense of vein crystals. **(c)** WNW-ESE-
779 striking subvertical joints (D2), which are spaced between 2 and 10 cm. **(d)** Low-displacement
780 fault surface (D2 and D3) coated with reddish calcite precipitates, which are characterized by
781 fiber slickenline morphology. **(e)** View of D3 characterized by optimally exposed fault
782 segments and foliated breccias, which rest above the fault surfaces. **(f)** High resolution hand
783 sample scan from D3 characterized by T2 and T3 veins. Note the crackle-like breccia texture
784 created by these veins.
785
786 **Figure 8.** Photographs and microphotographs of the secondary fault zone (domain 3, D3)
787 structures. **(a)** Foliated breccia affected by closely spaced foliation surfaces. **(b)** Foliated
788 breccias resting above a low-displacement fault surface. **(c)** Extensional fracture filled by

789 breccia. The fracture cuts across a low-displacement fault surface. **(d)** High resolution hand
790 sample scan of fault breccia characterized by chaotic texture. Note that the large clast on top is
791 affected by an inner crackle breccia texture. Note also T2 and T3 veins within clasts. **(e), (f)**
792 Microphotographs of foliated breccias taken under crossed polarized light. The G1 cement is
793 characterized by blocky to elongate-blocky calcite crystals, whereas acicular crystals
794 characterize the G2 fibrous cement. Note the depositional hiatus, which is characterized by
795 truncated crystal faces, between G1 and G2 cements.
796
797 **Figure 9. (a)** $\delta^{13}C$ (PDB) versus $\delta^{18}O$ (SMOW) diagram for 78 analyzed samples from various
798 carbonate rocks and mineralizations in the studied fault zone domains and surrounding area. **(b)**
799 Relative abundance of some major and minor elements of ultracataclasite and foliated
800 cataclasite from the principal fault (domain 1, D1) and host rock.
801
802 **Figure 10.** Cartoon showing the conceptual model of the evolution of a shallow (≤3 km)
803 extensional fault zone and seismic-related fluid circulation. **(a)** Burial-exhumation history of
804 the Apennine belt involving compression and post-collisional extension in the early stage and
805 in the late stage of fold-thrust belt development, respectively **(b)** In the first phase of fault zone
806 evolution, deformation and fault displacement are concentrated along the principal fault surface
807 (domain 1, D1), whereas less intense deformation is distributed within the damage zone
808 (domain 2 and 3, D2-D3). The isotope trend in the $\delta^{18}O$-$\delta^{13}C$ space indicates that calcite
809 precipitated from marine-derived fluids (brine and/or connate water) between ~3 km and ~1 km
810 depth and at temperature of ~68°C. **(c)** In the second phase of fault zone evolution, deformation
811 and fault displacement are distributed within the damage zone (domain 2 and 3, D2-D3). The
812 isotope trend in the $\delta^{18}O$-$\delta^{13}C$ space indicates that calcite precipitated from meteoric- and/or
813 groundwater-derived fluids at depth ≤ 1 km and at temperatures below 35°C. **(d)** Situation
814 between ~3 km and ~1 km depth. During co-seismic dilation, fluids instantaneously drop at

sub-hydrostatic pressure conditions within newly created dilatant fractures occurring in the damage zone (D2-D3). This process leads to calcite precipitation and mineralization. At the same time, localized and transient suprahydrostatic pressure condition can be generated along the principal fault surface (D1). After the co-seismic phase, fluids regain hydrostatic pressure conditions. **(e)** Situation at depth $\leq$ 1 km. During co-seismic dilation, fluids instantaneously drop at subhydrostatic pressure conditions within newly created dilatant fracture in the whole fault zone (D1-D2-D3). This process leads to calcite precipitation and mineralization. No evidence of localized and transient suprahydrostatic pressure conditions are present. After the co-seismic phase, fluids regain hydrostatic pressure conditions.

Figure 1

Click here to download high resolution image

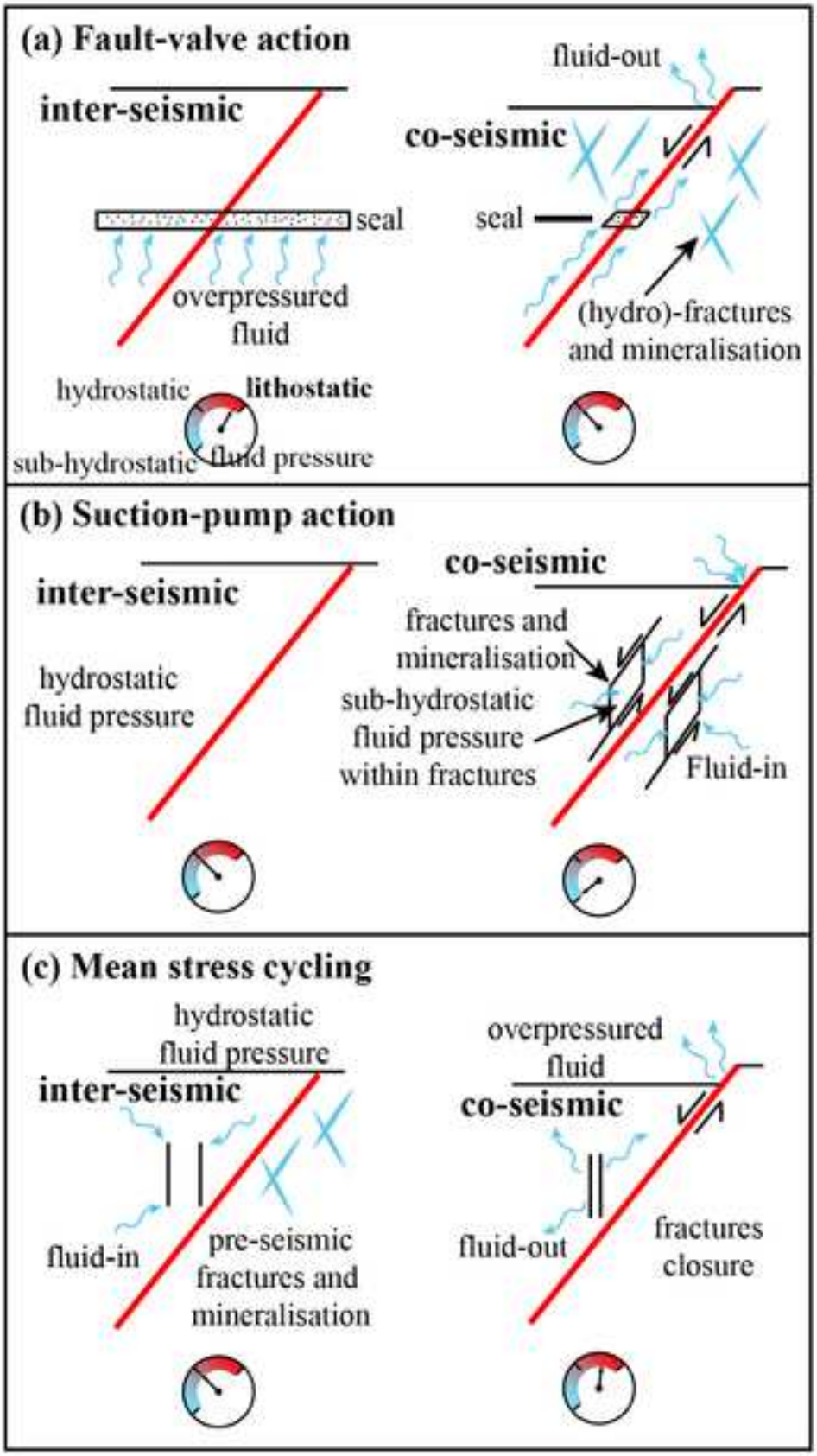

Fig. 1

single column

Figure 2

Click here to download high resolution image

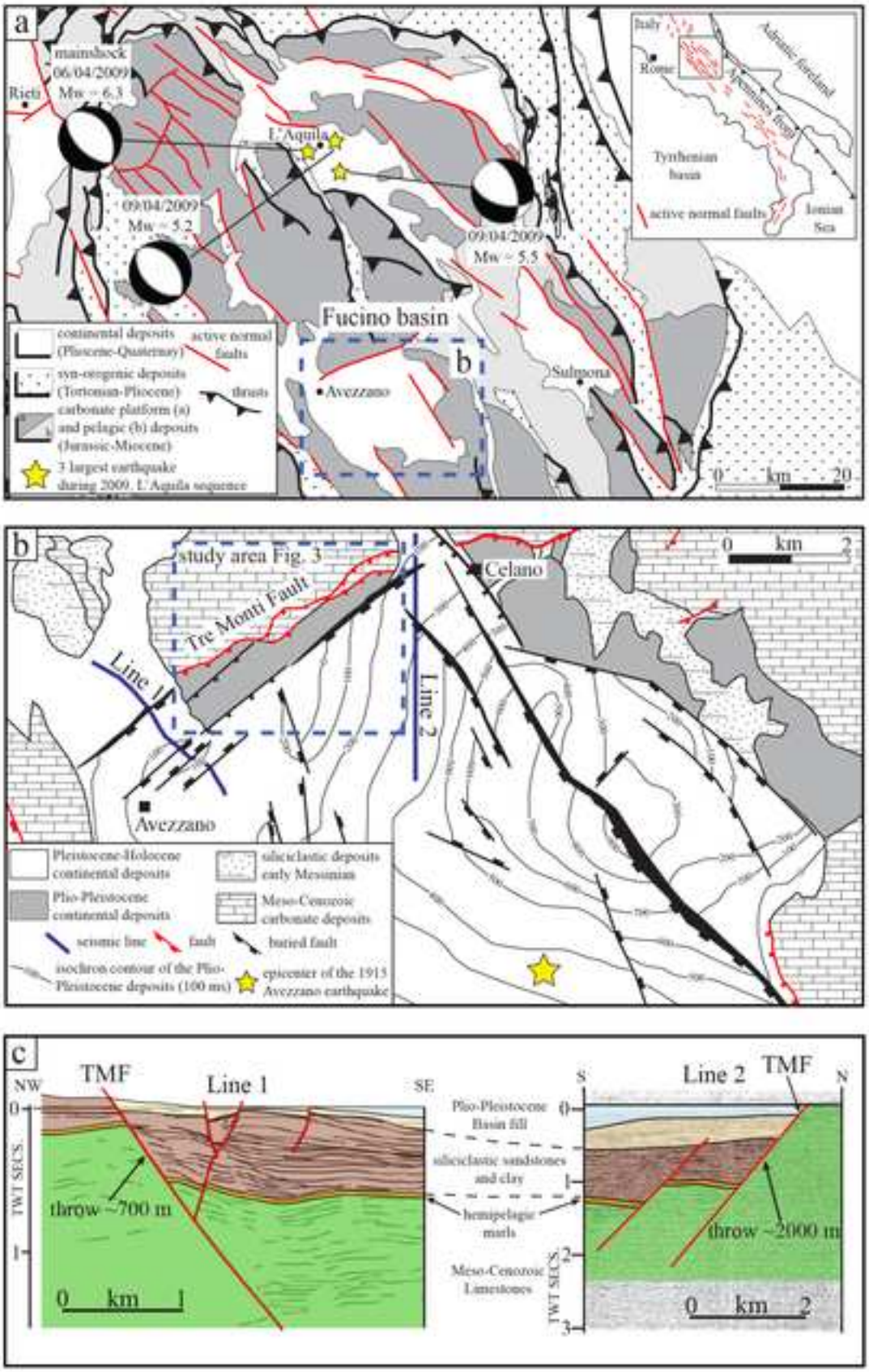

Fig. 2

1.5 column

Figure 3

Click here to download high resolution image

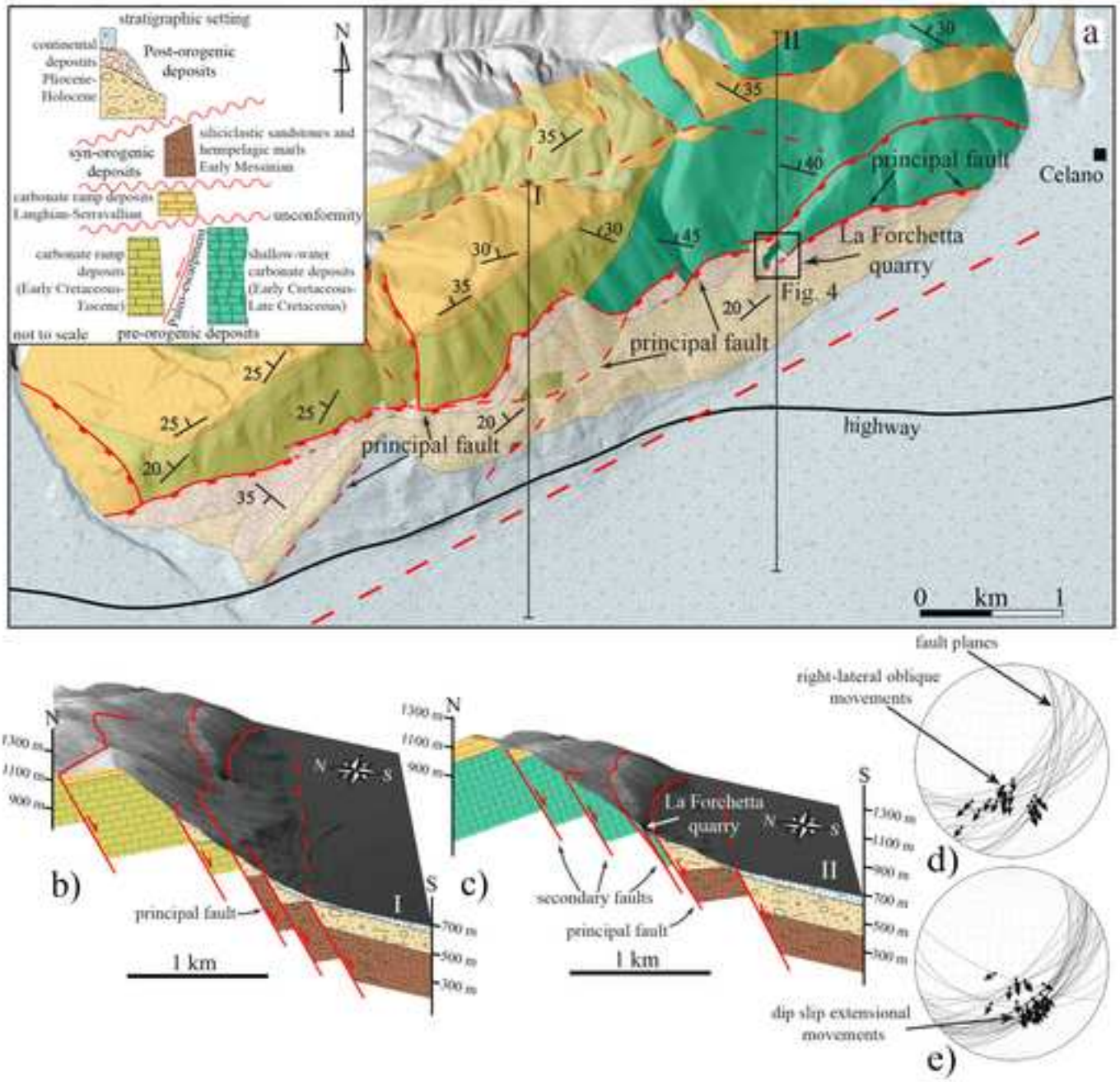

Fig. 3

2 column

Figure 4

Click here to download high resolution image

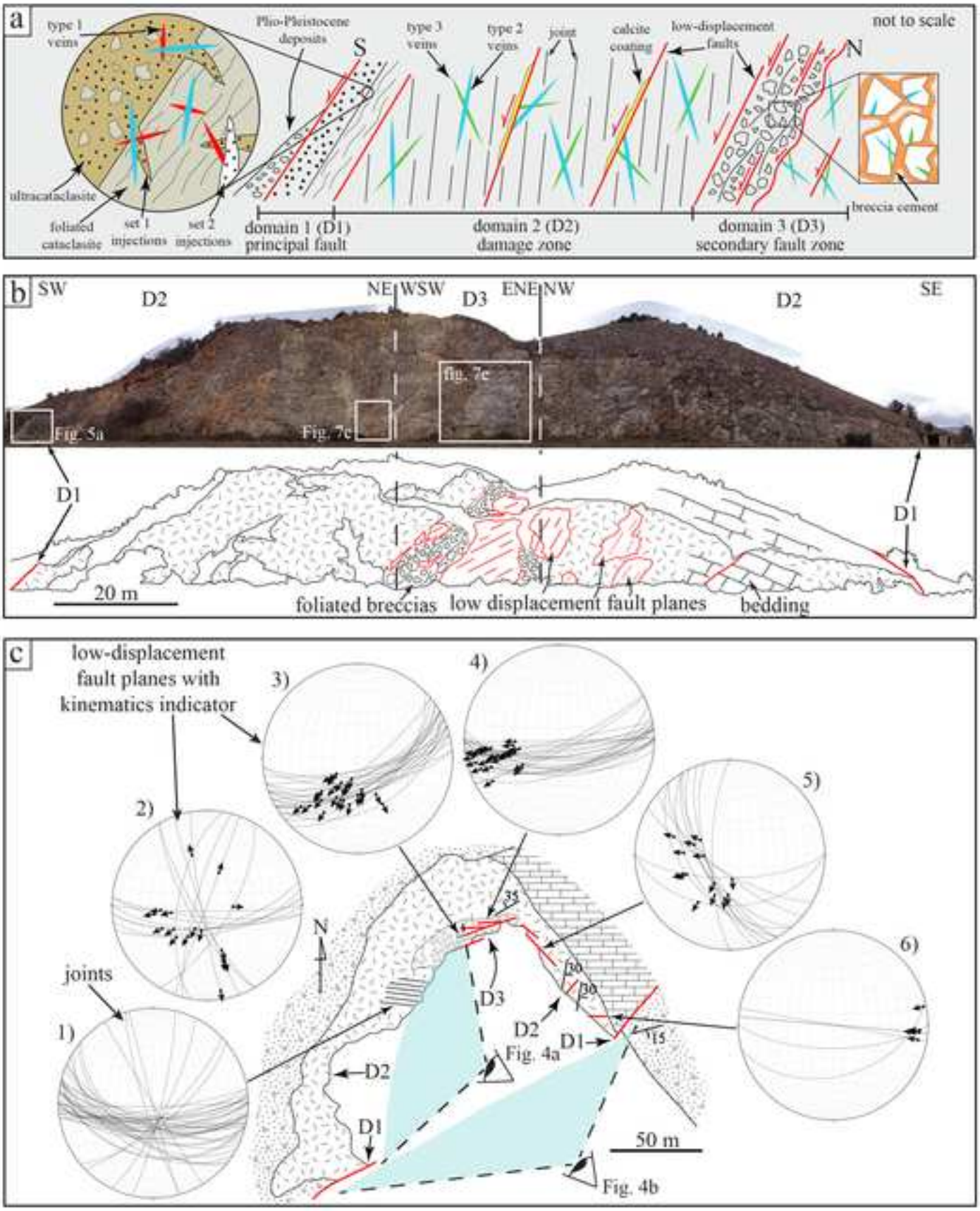

Fig. 4

2 column

Figure 5
Click here to download high resolution image

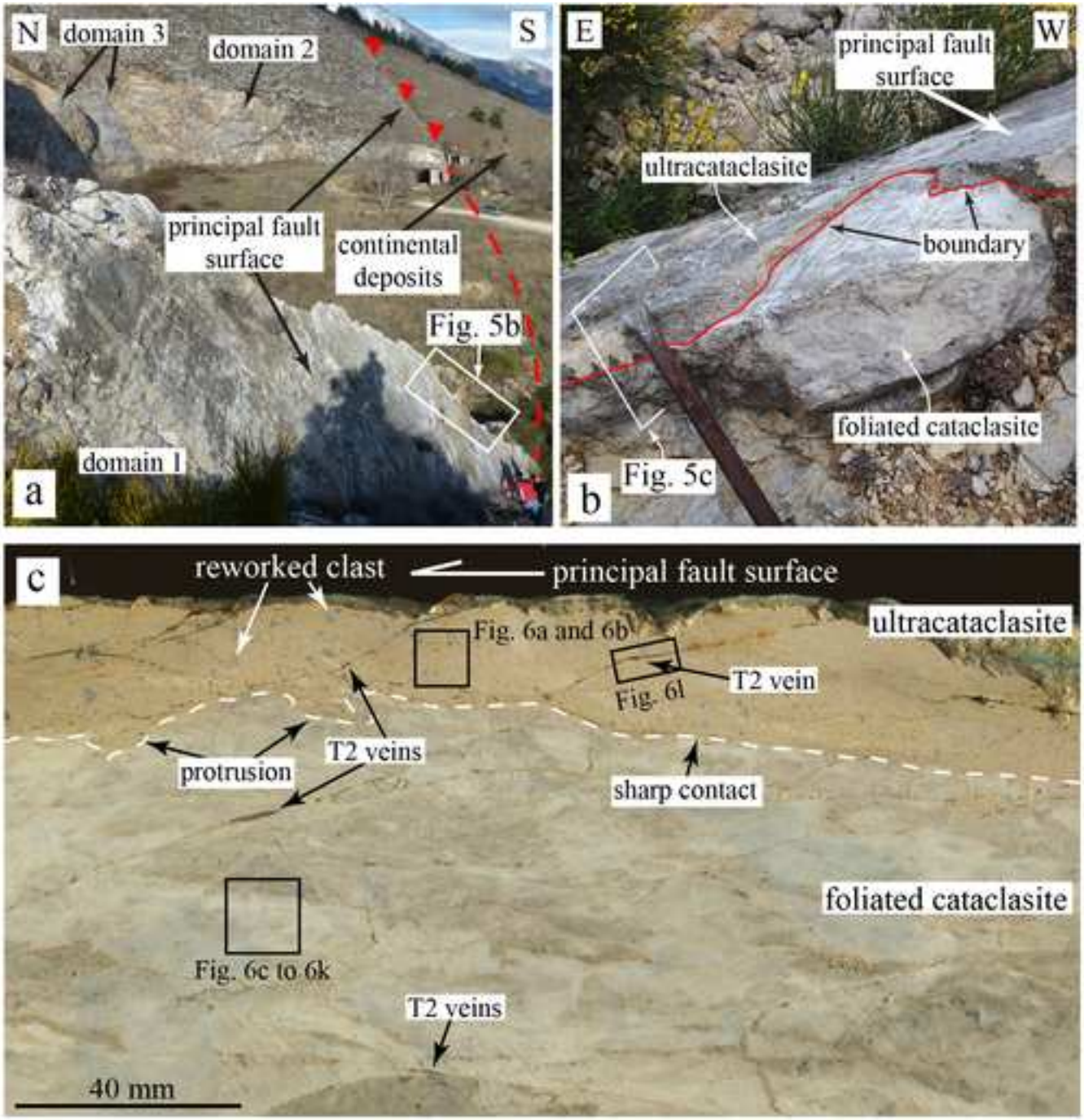

Fig. 5

1.5 column

Figure 6

Click here to download high resolution image

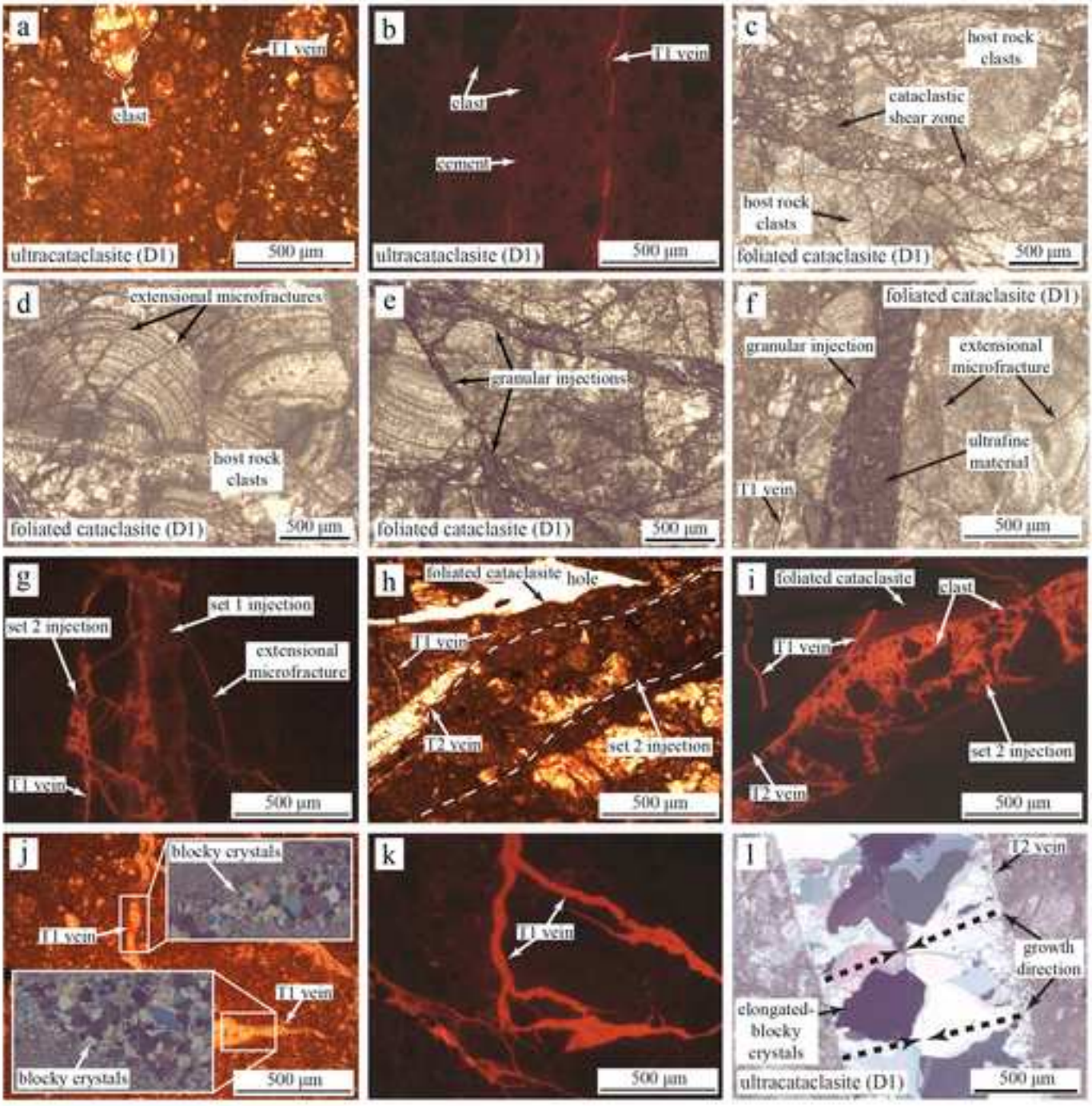

Fig. 6

2 column

Figure 7
Click here to download high resolution image

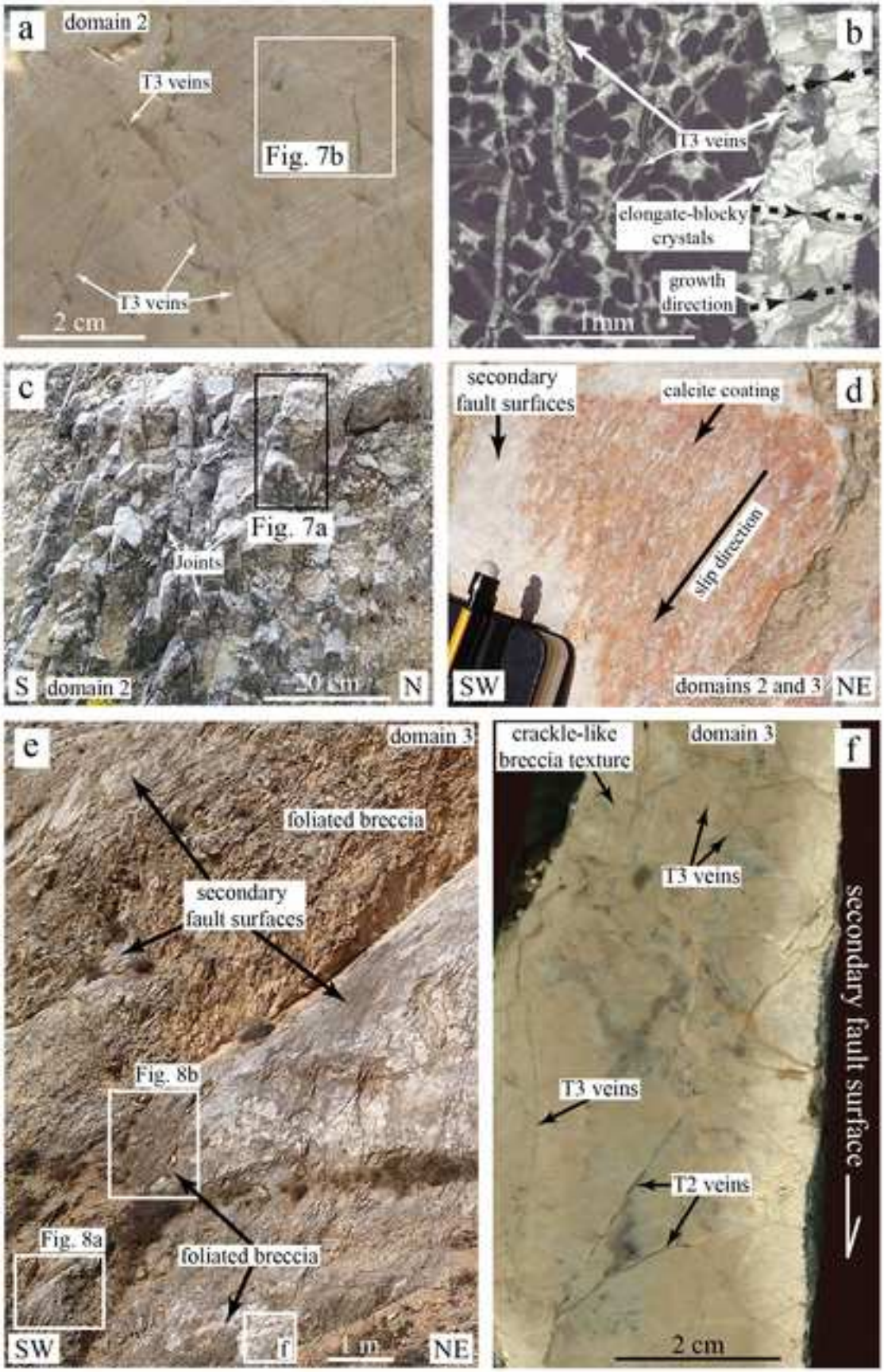

Fig. 7

1.5 column

Figure 8

Click here to download high resolution image

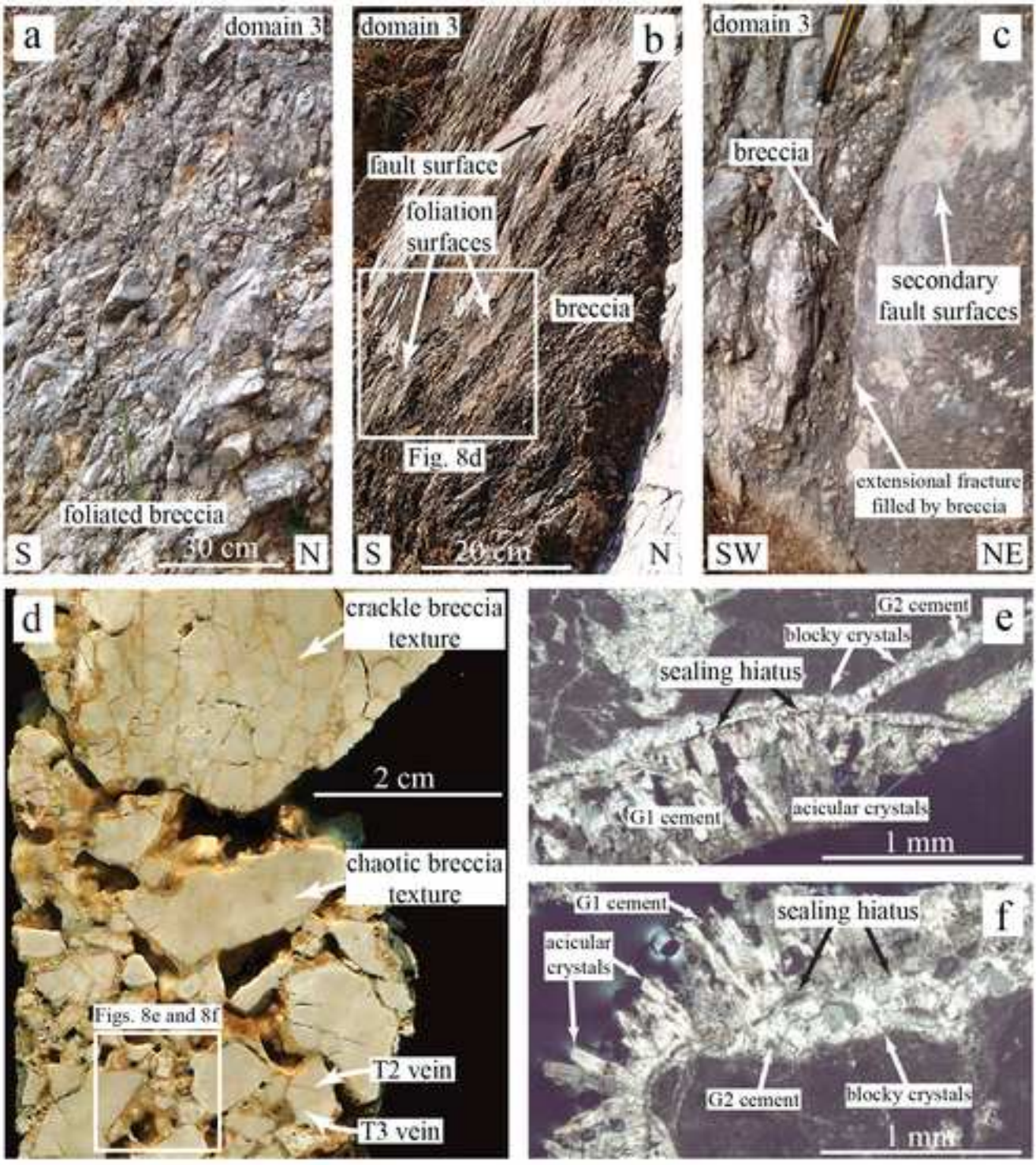

Fig. 8

1.5 column

Figure 9
Click here to download high resolution image

a)

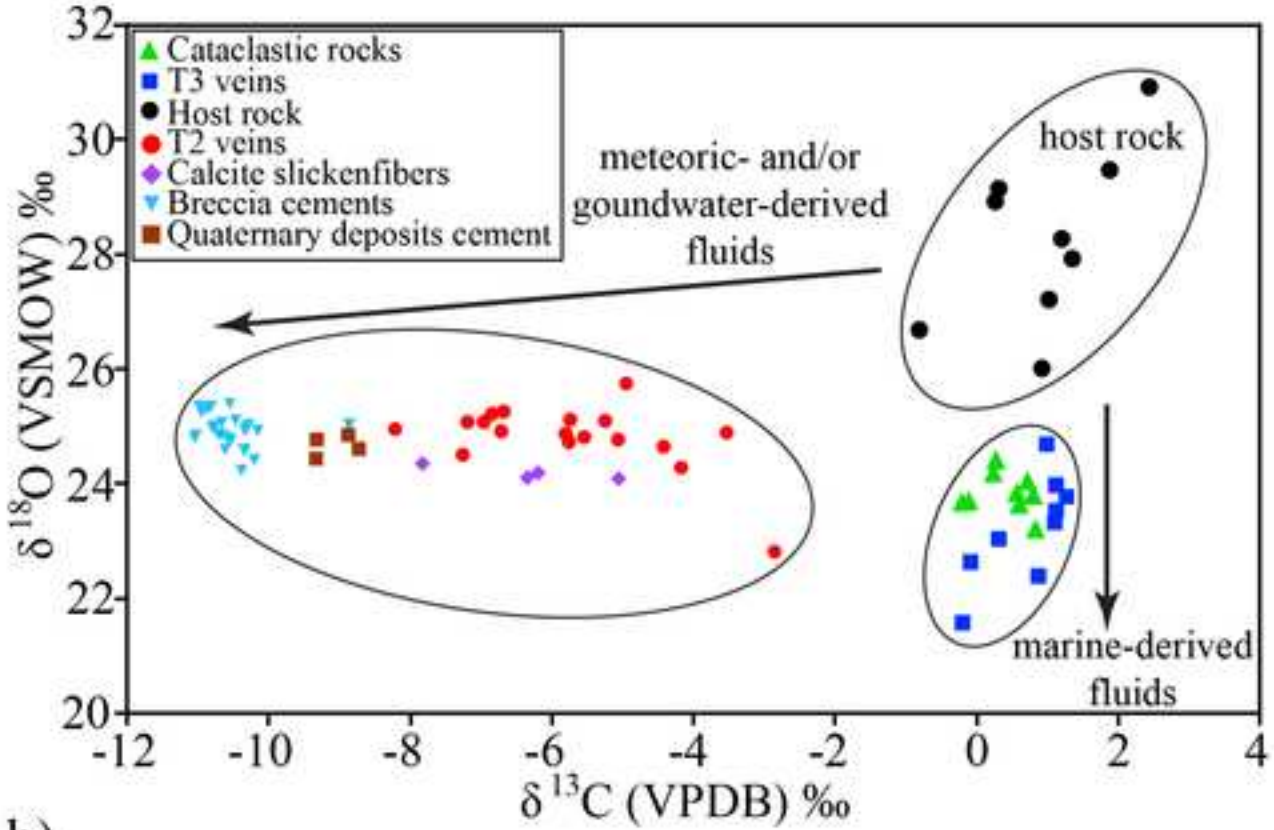

b)

Domain	Sample Name	CaO wt %	MgO wt %	MnO wt %	Sr ppm	LOI wt %
D1	Ultracataclasite 1	52.09	0.62	0.007	256	42.31
D1	Ultracataclasite 2	53.59	0.56	0.014	238	42.7
D1	Foliated cataclasite 3	54.61	0.63	0.003	191	43.23
D1	Foliated cataclasite 4	54	0.58	0.004	183	43.37
outside fault zone	Host rock 1	54.43	0.65	0.002	169	43.12
outside fault zone	Host rock 2	55.09	0.41	0.002	125	43.69

Fig. 9

Single column

Figure 10

Click here to download high resolution image

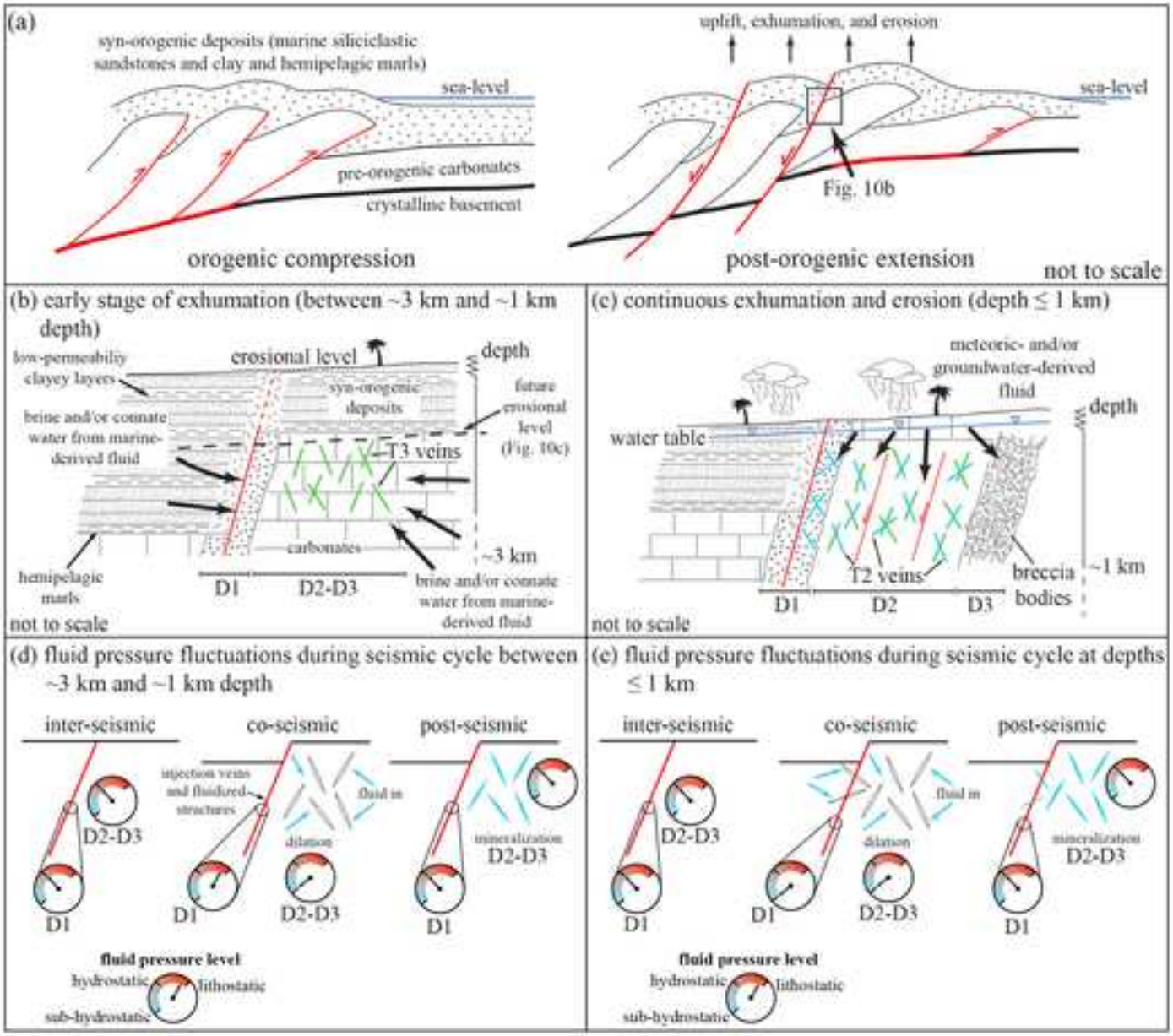

Fig. 10

2 column

Figure 1 (high-resolution)

Click here to download Figure (high-resolution): Smeraglia_Fig1.jpg

Figure 2 (high-resolution)

Click here to download Figure (high-resolution): Smeraglia_Fig2.jpg

Figure 3 (high-resolution)

Click here to download Figure (high-resolution): Smeraglia_Fig3.jpg

Figure 4 (high-resolution)

Click here to download Figure (high-resolution): Smeraglia_Fig4.jpg

Figure 5 (high-resolution)

Click here to download Figure (high-resolution): Smeraglia_Fig5.jpg

Figure 6 (high-resolution)

Click here to download Figure (high-resolution): Smeraglia_Fig6.jpg

Figure 7 (high-resolution)

Click here to download Figure (high-resolution): Smeraglia_Fig7.jpg

Figure 8 (high-resolution)

Click here to download Figure (high-resolution): Smeraglia_Fig8.jpg

Figure 9 (high-resolution)

Click here to download Figure (high-resolution): Smeraglia_Fig9.jpg

Figure 10 (high-resolution)

Click here to download Figure (high-resolution): Smeraglia_Fig10.jpg

Table S1

Click here to download Supplementary material for online publication only: Smeraglia_TableS1.docx

Table S2

Click here to download Supplementary material for online publication only: Smeraglia_TableS2.docx

Table S3

Click here to download Supplementary material for online publication only: Smeraglia_TableS3.docx